Front. Phys.
https://doi.org/10.15302/frontphys.2027.055301
CN 11-5994/O4
ISSN 2095-0462

REVIEW ARTICLE

Classification of valley polarization and multifield tuning in altermagnets

Kai Wei[1, 2,*], Yanchao She[1,3,*], Pengqiang Dong[1,2], Hengzhe Fu[1], Fengyu Ran[1], Ping Li[1, 2, 3, 4, †]

[1]State Key Laboratory for Mechanical Behavior of Materials, School of Materials Science and Engineering, Xi'an Jiaotong University, Xi'an 710049, China

[2]Shaanxi Yanyi Titanium Industry Company Limited, Baoji 721001, China

[3]Department of Physics and Electronic Engineering, Tongren University, Tongren 554300, China

[4]Hefei National Research Center for Physical Sciences at the Microscale, University of Science and Technology of China, Hefei 230026, China

[*]These authors contributed equally to this work.

Corresponding author. E-mail: [†]pli@xjtu.edu.cn

Received September 25, 2026; accepted November 16, 2026

Abstract

As the third electronic degree of freedom beyond charge and spin, the valley degree of freedom has recently garnered substantial interest, owing to its exceptional potential for enabling next-generation devices that feature ultrafast operation, ultrahigh storage capacity, low energy consumption, and nonvolatile functionality. The utilization of the valley index as an information carrier hinges on the controlled manipulation of valley carriers, which is a prerequisite for achieving valley polarization. Intrinsic spontaneous valley polarization originates from symmetry breaking and spin-orbit coupling. In this review, we first introduce the characteristics of altermagnets and the valley physics in these materials from the perspective of symmetry. Then, based on the symmetry origins of valley polarization, we divide the currently known spontaneous valley polarization into three classes and list the candidate materials. Third, we discuss in detail the tuning of altermagnetic valley polarization via strain, electric field, electrostatic potential, magnetic field, interlayer stacking, and proximity effect, along with the device prototypes for spintronics and valleytronics that are built upon these effects. Finally, we anticipate the advancement of altermagnetic valleytronics through expanding the database of altermagnets exhibiting valley polarization, the construction of a coupled Hamiltonian incorporating multiple degrees of freedom, and the investigation of prototype valleytronics and spintronics devices.

Keywords valley polarization classification, altermagnet valley polarization, anomalous valley Hall effect, multifield tunable valley polarization

© Higher Education Press 2026

Just Accepted

This is a "Just Accepted" manuscript, which has been examined by the peer-review process and has been accepted for publication. A "Just Accepted" manuscript is published online shortly after its acceptance, which is prior to technical editing and formatting and author proofing. Higher Education Press (HEP) provides "Just Accepted" as an

optional and free service which allows authors to make their results available to the research community as soon as possible after acceptance. After a manuscript has been technically edited and formatted, it will be removed from the "Just Accepted" Web site and published as an Online First article. Please note that technical editing may introduce minor changes to the manuscript text and/or graphics which may affect the content, and all legal disclaimers that apply to the journal pertain. In no event shall HEP be held responsible for errors or consequences arising from the use of any information contained in these "Just Accepted" manuscripts. To cite this manuscript please use its Digital Object Identifier (DOI®), which is identical for all formats of publication.

Classification of valley polarization and multifield tuning in altermagnets

Kai Wei,[1,2,*] Yanchao She,[1,3,*] Pengqiang Dong,[1,2] Hengzhe Fu,[1] Fengyu Ran,[1] and Ping Li[1,2,3,4,†]

[1] *State Key Laboratory for Mechanical Behavior of Materials, School of Materials Science and Engineering, Xi'an Jiaotong University, Xi'an, Shaanxi, 710049, People's Republic of China*

[2] *Shaanxi Yanyi Titanium Industry Company Limited, Baoji, Shaanxi, 721001, People's Republic of China*

[3] *Department of Physics and Electronic Engineering, Tongren University, Tongren, Guizhou, 554300, People's Republic of China*

[4] *Hefei National Research Center for Physical Sciences at the Microscale, University of Science and Technology of China, Hefei, Anhui, 230026, People's Republic of China*

(Dated: October 31, 2026)

As the third electronic degree of freedom beyond charge and spin, the valley degree of freedom has recently garnered substantial interest, owing to its exceptional potential for enabling next-generation devices that feature ultrafast operation, ultrahigh storage capacity, low energy consumption, and nonvolatile functionality. The utilization of the valley index as an information carrier hinges on the controlled manipulation of valley carriers, which is a prerequisite for achieving valley polarization. Intrinsic spontaneous valley polarization originates from symmetry breaking and spin-orbit coupling. In this review, we first introduce the characteristics of the altermagnets and the valley physics in these materials from the perspective of symmetry. Then, based on the symmetry origins of valley polarization, we divide the currently known spontaneous valley polarization into three classes and enumerate the candidate materials. Third, we discussed in detail the tuning of altermagnet valley polarization via strain, electric field, electrostatic potential, magnetic field, interlayer stacking, and proximity effect, along with the device prototypes for spintronics and valleytronics that are built upon this. Finally, we anticipate the advancement of altermagnet valleytronics through the improvement of the database for valley-polarized altermagnets, the construction of a coupled Hamiltonian incorporating multiple degrees of freedom, and the investigation of prototype valleytronics and spintronics devices.

Keywords valley polarization classification, altermagnet valley polarization, anomalous valley Hall effect, multifield tunable valley polarization

CONTENTS

1 Introduction

2 The characteristics of altermagnets and valleytronics

2.1 The characteristics of altermagnets

2.2 Altermagnets classification

2.3 The valley physics in altermagnets

3 Valley polarization classification

3.1 Type I valley polarization: ferromagnetic materials with the broken time-reversal symmetry

3.2 Type II valley polarization: ferroelectric materials with the broken spatial inversion symmetry

3.3 Type III valley polarization: materials with the broken lattice symmetry

3.3.1 Type III valley polarization in non-magnetic materials

3.3.2 Type III valley polarization in magnetic materials

4 Multifield tunable valley polarization in altermagnets

4.1 Strain tunable valley polarization

4.2 Electric field tunable valley polarization

4.3 Electrostatic potential tunable valley polarization

4.4 Magnetic field tunable valley polarization

4.5 Interlayer stacking tunable valley polarization

4.6 Proximity effect tunable valley polarization

5 Conclusions and perspectives

Declarations

* These authors contributed equally to this work

† pli@xjtu.edu.cn

Acknowledgements

References

1. INTRODUCTION

In the research landscape of condensed matter physics, magnetic materials have long been categorized into two distinct camps: ferromagnetic (FM) and antiferromagnetic (AFM) materials. Both have played a crucial role in advancing technology [1–3]. The FM materials are known for their macroscopic magnetization, which arises from the parallel alignment of magnetic moments. Its dominance spans the development of permanent magnets, magnetic sensors, and magnetic storage [1, 2, 4, 5]. In particular, the giant magnetoresistance (GMR) effect, arising from its spin-split band structure, earned the 2007 Nobel Prize in Physics [6, 7]. Nevertheless, the inherent characteristics of FM materials present considerable obstacles for FM spintronic devices, especially regarding stability, scalability, and dynamic behavior. These limitations make them difficult to integrate into advanced electronic systems. Specifically, the stray field effect of FM materials and the GHz-level magnetic dynamics frequency severely restrict the high-density integration and ultra-high-speed operation of the devices [8, 9]. In conventional AFM materials, the fully compensated antiparallel alignment of magnetic moments results in a zero net magnetic moment, which endows them with remarkable robustness against external magnetic perturbations and eliminates stray fields [10–15]. Moreover, the AFM materials possess THz-level intrinsic frequencies, opening up new directions for the application of spintronics [16, 17]. However, the spin-degenerate energy band structure in its reciprocal space is incompatible with the GRM effect, which has long consigned it to the predicament of possessing immense theoretical potential yet facing formidable challenges in practical application. To transcend the application constraints of collinear FM and AFM materials in spintronics, researchers have been seeking novel materials that merge the desirable properties of both FM and AFM orders. A new magnetic phase was born: altermagnetism [18, 19].

Altermagnetism is a newly discovered class of collinear magnets beyond traditional ferromagnetism and antiferromagnetism. It features spin splitting similar to that of a ferromagnet, while maintaining the AFM-like order with zero net magnetization [18, 19]. Noted that it exhibits non-relativistic spin splitting, despite its compensated collinear magnetic configuration [20–24]. Moreover, altermagnetism is associated with the breaking of time-reversal symmetry ($\mathcal{T}$) and the lifting of Kramers' degeneracy. These distinctive features of altermagnets give rise to rich physical phenomena. The GMR and tunneling magnetoresistance (TMR) effects are observed in altermagnets due to the characteristic of spin splitting [25–30]. Moreover, the anomalous Hall effect that is comparable to that in FM materials has been reported [31–36]. Additionally, novel transport properties such as nonlinear transport [37–40], anomalous Nernst effect [41, 42], and magneto-optical Kerr effect [43–46] have also been discovered in altermagnets. The spin splitter torque, a novel type of torque, has been both theoretically predicted [47] and experimentally confirmed [48, 49] in altermagnets. In addition, the chiral Majorana fermions or Majorana zero energy modes are reported to emerge in altermagnet-based heterojunctions [50, 51].

It is well known that electrons possess two intrinsic degrees of freedom: charge and spin. Based on these two degrees of freedom, today's widely used electronics and the increasingly mature field of spintronics have been developed. A natural question arises: could there be other degrees of freedom for electrons in solids, apart from charge and spin? The answer is in the affirmative. In many crystal structures, such as semiconductors like silicon, germanium, and gallium arsenide, as well as insulating materials like diamond, electrons also possess a new usable degree of freedom known as the valley [52–56]. Valley specifically refers to the local extremum in the momentum space of electronic crystals, such as the conduction band minimum and valence band maximum at the local region [57–59]. Since the successful preparation of two-dimensional graphene [60], single-atom-layer two-dimensional valley materials of atomic thickness, such as graphene and silicene, have been extensively studied [61–65]. The most notable feature is that the two inequivalent valleys (K and K') have Berry curvatures of opposite signs. This leads to opposite signs of the Berry-curvature-induced transport coefficients and optical selection rules, providing a theoretical basis for valley polarization modulation by optical fields. Since the theoretical scheme has yet to be experimentally confirmed, and breaking the lattice symmetry of graphene is extremely difficult. Hence, graphene is not an ideal material for valleytronics. Quickly, researchers have shifted their focus to 2H-phase transition metal chalcogenides (TMDs), such as MoS_2 [66, 67]. Unlike graphene, monolayer TMDs are direct band gap materials and naturally break inversion symmetry ($\mathcal{P}$). Therefore, the valley-resolved optical selection rules and valley Hall effect were quickly observed experimentally [68, 69]. Even though the non-equivalent valleys are distinct in momentum space for the 2H-TMDs system, they remain energy degenerate. Consequently, valley polarization cannot be realized. The achievement of valley polarization is beneficial for the development of valleytronics and spintronics. Therefore, a series of methods for realizing valley polarization have been proposed, such as magnetic proximity effect [70–74], magnetic atom doping [75–78], external magnetic fields [79–83], and circularly polarized light [68, 69, 84, 85]. It is worth noting that this is not an intrinsic property of the material, which is unfavorable for the manipulation of the valley degree of freedom. In 2016, analogous to spontaneous magnetization in ferromagnets and spontaneous polar-

ization in ferroelectrics (FE), Duan *et al.* proposed spontaneous valley polarization and named this class of materials "ferrovalley materials" [86]. Up to now, theory has predicted a series of ferrovalley materials, such as LaX_2 (X = Br, I) [87–89], FeX_2 (X = Cl, Br, I) [90–92], VX_2Y_4 (X = C, Si, Ge, Sn, Pb; Y = N, P, As) [93–98], YX_2 (X = Cl, Br, I) [99–101], GdX_2 (X = Cl, I) [102–104], Nb_3I_8 [105], MnBr [106], $MnPX_3$ (X = Se, Te) [107–109], XY (X = K, Rb, Cs; Y = N, P, As, Sb, Bi) [110], CeI_2 [111], Cr_2COOH [112], XY_2 (X = Ru, Os; Y = Cl, Br) [113], and so on.

Since the advent of altermagnets, valley polarization research has increasingly concentrated on these materials. Altermagnetic ferrovalleys differ from ferromagnetic ferrovalley materials. The key difference is that their valley degeneracy originates from different symmetry protections. Ferromagnetic ferrovalleys are primarily protected by the $\mathcal{P}$ symmetry, whereas altermagnetic ferrovalleys are mainly protected by mirror symmetry ($\mathcal{M}$). In this review, we first introduce the characteristics of altermagnets and valleytronics. Then, we discuss three types of intrinsic valley polarization, which are classified by the symmetry responsible for valley degeneracy protection. In addition, we summarize the multifield manipulation of valley polarization in altermagnets, including strain, electric field, electrostatic potential, magnetic field, interlayer stacking and proximity effect. Although our understanding of valley polarization in altermagnets is still in its early stages, this field has already become a fertile ground for theoretical exploration and holds great promise for opening new avenues in the development of valleytronic and spintronic devices.

2. THE CHARACTERISTICS OF ALTERMAGNETS AND VALLEYTRONICS

Altermagnets, due to their combination of ferromagnetic and antiferromagnetic properties, exhibit unique application prospects in spintronic devices. Furthermore, altermagnets enable an elegant merging of spintronics and valleytronics through spin-valley locking. The combination of altermagnets and the valley degree of freedom has brought new vitality to spintronics. It is expected to resolve the core contradictions of traditional magnetic storage technology, namely, slow read/write speed and low integration density. It also provides a solid physical foundation and a feasible technical platform for the future development of information processing and storage technologies featuring ultra-high speed, ultra-high density, and ultra-low power consumption.

2.1. The characteristics of altermagnets

Conventionally, two mechanisms can induce spin splitting in electronic bands: relativistic spin-orbit coupling (SOC), which produces Rashba-type and Dresselhaus-type splitting [116, 117], and non-relativistic exchange coupling, exemplified by Zeeman splitting in ferromagnets [118]. Here we mainly focus on non-relativistic spin splitting. In all collinear magnets, the spin-only symmetry $[\mathcal{C}_\infty||E]$ ensures that spin remains a good quantum number and does not depend on momentum k. Here, $\mathcal{C}_\infty$ represents arbitrary rotations of spin about the common spin axis, while E is the identity operation in real space. Thus, the band energy can be expressed as a function of both wavevector k and spin s: $E(k, s)$. Another spin-only group is $\bar{\mathcal{C}}_2$ in collinear magnets. It denotes a twofold rotation perpendicular to the collinear spin axis. Since spin-space inversion occurs by time reversal [119–121], it is inherently paired with the $\mathcal{T}$ operation in real space. Therefore, it denote as $[\bar{\mathcal{C}}_2||\mathcal{T}]$. The combination of $\bar{\mathcal{C}}_2$ symmetry and the collinear symmetry $\mathcal{C}_\infty$ gives rise to nonrelativistic $\mathcal{P}$ symmetry in the band structure [122], thereby enforcing $E(k, s) = E(-k, s)$. Therefore, the bands have even parity with respect to momentum near the Γ point. The foregoing analysis indicates that, for any collinear magnetic system, $\mathcal{P}$ symmetry leaves the nonrelativistic bands invariant, regardless of whether the system exhibits real-space inversion symmetry. If a collinear magnet possesses $[\mathcal{C}_2||\mathcal{P}]$ symmetry, then its spin bands are Kramers degenerate throughout the entire Brillouin zone. This degeneracy stems from the fact that $[\mathcal{C}_2||\mathcal{P}][\mathcal{C}_2||\mathcal{T}]$ leads to $E(k, s) = E(k, -s)$, which is the same as $\mathcal{PT}$ symmetry. Furthermore, the symmetry designated as $[\mathcal{C}_2||E]/[\mathcal{C}_2||\tau]$ (τ signifies translational symmetries) similarly enforces the condition $E(k, s) = E(k, -s)$.

As shown in Fig. 1, the three typical magnetic phases are distinguished through symmetry operations. For the FM phase, the spin Laue group is represented by the notation $\mathbf{R}_s^{\mathrm{I}} = [E||\mathbf{G}]$, where E and $\mathbf{G}$ denote the identity operation in spin space and crystallographic Laue group of the non-magnetic lattice, respectively. Therefore, the $\mathcal{T}$ symmetry is fully broken [123, 124]. As shown in Fig. 1(a), the $\mathbf{R}_s^{\mathrm{I}}$ groups do not give rise to spin degeneracy of $E(k, s)$ at any k-point. Since time reversal reverses all spin directions, while the symmetry group $[E||\mathbf{G}]$ lacks any operation that can reverse spins or compensate for this reversal via a real-space transformation. Accordingly, the time-reversed state cannot be restored to the original ferromagnetic configuration, leading to full spin splitting of the energy bands. For the AFM phase, the spin Laue group is expressed as $\mathbf{R}_s^{\mathrm{II}} = [E||\mathbf{G}] + [\mathcal{C}_2||\mathbf{G}]$. Relative to FM phase, AFM possess an extra symmetry operation that combines a twofold spin rotation ($\mathcal{C}_2$) with a real-space symmetry $\mathbf{G}$. As shown in Fig. 1(b), the opposite magnetic sublattices are connected by combined operations of $\mathcal{T}$ symmetry and spatial operations such as $\mathcal{P}$ or τ symmetries, which result in spin degeneracy throughout the entire Brillouin zone with SOC effect [10, 125, 126]. For the altermagnet phase, the spin Laue group is described as $\mathbf{R}_s^{\mathrm{III}} = [E||\mathbf{H}] + [\mathcal{C}_2||\mathrm{A}][E||\mathbf{H}] = [E||\mathbf{H}] + [\mathcal{C}_2||\mathbf{G} - \mathbf{H}]$, where $\mathbf{H}$ represents a halving subgroup of the nonmagnetic crystalline symmetry group $\mathbf{G}$.

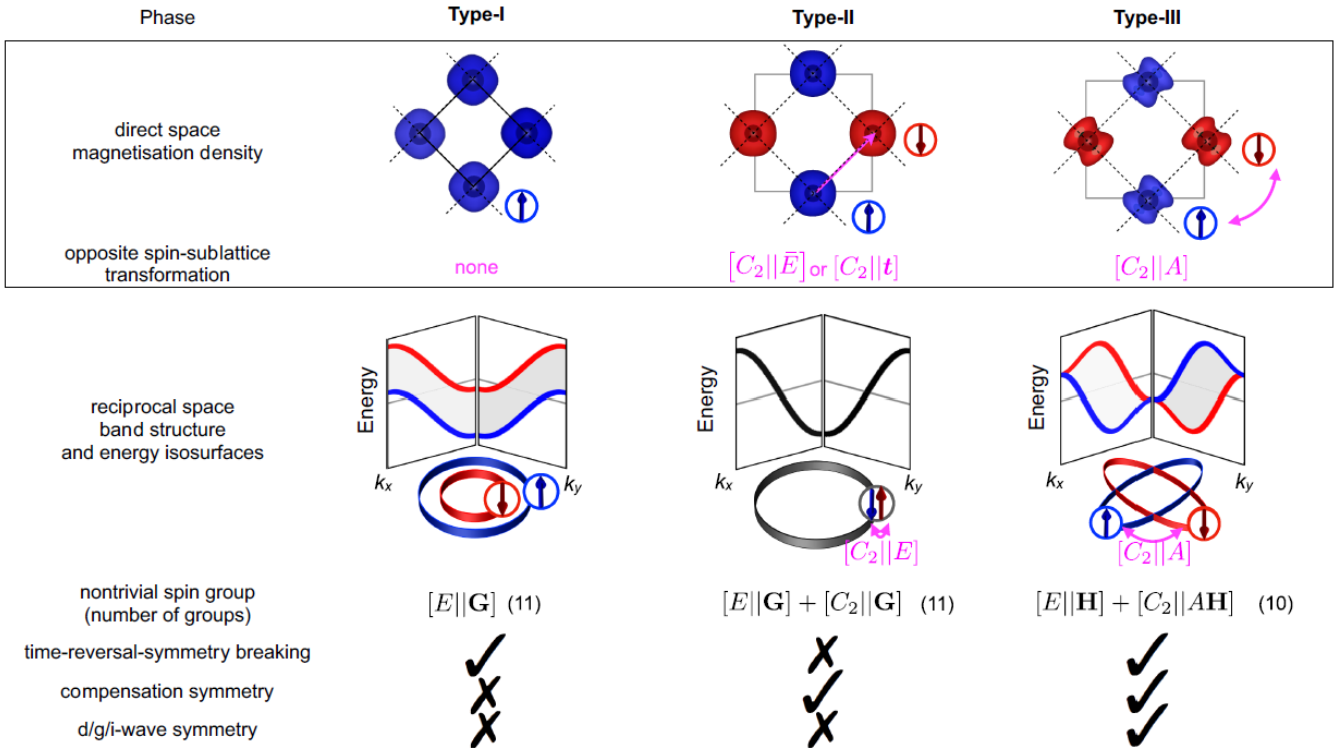


FIG. 1. The schematic diagram of three non-relativistic spin splitting in collinearmagnetic phases [18]. First line: schematic diagram of collinear spin arrangements and magnetization density. Middle row: schematic diagram of band structures and corresponding iso-energy surfaces. Bottom line: the spin Laue group of three collinearmagnetic states and presence/absence of symmetry.

It consists of real-space symmetry operations that hold within each magnetic sublattice once the magnetic order is included, namely operations that do not exchange sublattices of opposite spin. Consequently, the $[E||\mathbf{H}]$ component denotes the spatial symmetry operations that preserve the integrity of individual magnetic sublattices. As shown in Fig. 1(c), the residual symmetries impose restrictions on the shape of anisotropic spin-density distributions and their angular dependence, consequently giving rise to momentum-dependent spin polarizations, such as d-, g-, and i-wave spin splittings [127]. The remaining real-space symmetries of the nonmagnetic group form the set $\mathbf{G}$ - $\mathbf{H}$ = A$\mathbf{H}$, which contains operations that exchange sublattices with opposite spins. The lifting of spin degeneracy is fundamentally due to composite symmetry operations denoted $[\mathcal{C}_2||\mathrm{A}\mathbf{H}]$. Specifically, when a sublattice exchange in real space is accompanied by a twofold spin rotation ($\mathcal{C}_2$), the $\mathcal{T}$ symmetry is broken at the band-structure level, while the system retains a zero net magnetization [20]. The nonrelativistic spin splitting observed in altermagnets originates from this cooperative mechanism.

2.2. Altermagnets classification

The classification of altermagnets, which is mainly based on the spin-momentum locking characteristics, is crucial for understanding their physical properties. Mainly, the Litvin's notation is used for the spin Laue group [120], where the upper index 1 denotes the spin-space identity, and the upper index 2 denotes the rotation symmetry $\mathcal{C}_2$ in spin-space. Notably, they are derived from only eight distinct crystallographic Laue groups (Planar: 2/m, mmm, 4/m, 6/m; Bulk: $\bar{1}$, $\bar{3}$, $\bar{3}$m, m$\bar{3}$). Therefore, the altermagnets contain twelve nontrivial spin Laue groups, including ${}^{2}2/{}^{2}\mathrm{m}_{x}$, ${}^{2}\mathrm{m}{}^{2}\mathrm{m}{}^{1}\mathrm{m}$, ${}^{2}4/{}^{1}\mathrm{m}$, ${}^{2}4/{}^{1}\mathrm{m}{}^{2}\mathrm{m}{}^{1}\mathrm{m}$, ${}^{1}4/{}^{1}\mathrm{m}{}^{2}\mathrm{m}{}^{2}\mathrm{m}$, ${}^{1}\bar{3}{}^{2}\mathrm{m}$, and ${}^{1}6/{}^{1}\mathrm{m}{}^{2}\mathrm{m}{}^{2}\mathrm{m}$ for planar system, ${}^{2}2/{}^{2}\mathrm{m}$, ${}^{1}\bar{3}{}^{2}\mathrm{m}$, ${}^{2}6/{}^{2}\mathrm{m}$, ${}^{2}6/{}^{2}\mathrm{m}{}^{2}\mathrm{m}{}^{1}\mathrm{m}$, and ${}^{1}\mathrm{m}{}^{1}\bar{3}{}^{2}\mathrm{m}$ for bulk system. As shown in Fig. 2, altermagnets can be classified into d-, g-, and i-wave types on the basis of spin-momentum locking [18, 128]. When a closed loop is traced around the Γ-point in a plane normal to a spin-degenerate nodal surface intersecting Γ, the spin is rotated by 360° following two discrete sign flips. Notably, the total number of such rotations defines a characteristic, namely an even integer. As shown in Fig. 2, the d-, g-, and i-wave classifications correspond to characteristic integers of 2, 4, and 6, respec-

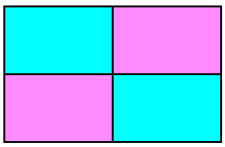
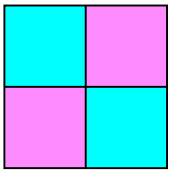
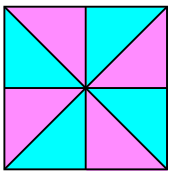
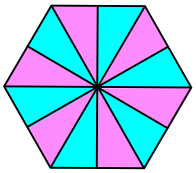
Spin Laue group	Spin-momentum locking (k_x, k_y)	Candidate material
${}^{2}2/{}^{2}m_x$		VF_4 [129,130]
${}^{2}m{}^{2}m{}^{1}m$		Bilayer $MnPS_3$ [131]
${}^{2}4/{}^{1}m$		
${}^{2}4/{}^{1}m{}^{2}m{}^{1}m$		V_2Se_2O [22]
${}^{1}4/{}^{1}m{}^{2}m{}^{2}m$		$VP_2H_8(NO_4)_2$ [128]
${}^{1}\bar{3}{}^{2}m$		$V_2P_2S_3Se_3$ [132]
${}^{1}6/{}^{1}m{}^{2}m{}^{2}m$		

FIG. 2. Based on spin-momentum locking, altermagnets are classified into three types, including d-, g-, and i-wave. The corresponding spin group symmetries and candidate materials are presented.

tively. Here, we focus on the features and symmetries of two-dimensional altermagnets. For the d-wave altermagnet, it exhibits twofold symmetry. Their corresponding spin Laue group are ${}^{2}2/{}^{2}\mathrm{m}_x$, ${}^{2}\mathrm{m}{}^{2}\mathrm{m}{}^{1}\mathrm{m}$, ${}^{2}4/{}^{1}\mathrm{m}$, and ${}^{2}4/{}^{1}\mathrm{m}{}^{2}\mathrm{m}{}^{1}\mathrm{m}$, which representative candidate materials are VF_4 [129, 130], bilayer $MnPS_3$ [131], and V_2Se_2O [22], respectively. When the characteristic integer becomes 4, the g-wave altermagnet has fourfold rotational symmetry in the momentum space. The corresponding nontrivial spin Laue group is ${}^{1}4/{}^{1}\mathrm{m}{}^{2}\mathrm{m}{}^{2}\mathrm{m}$,, and the candidate materials include $VP_2H_8(NO_4)_2$ [128]. Additionally, for the i-wave altermagnetic phase possessing sixfold rotational symmetry, two distinct spin Laue groups are identified, designated as $1\bar{3}{}^{2}\mathrm{m}$ and ${}^{1}6/{}^{1}\mathrm{m}{}^{2}\mathrm{m}{}^{2}\mathrm{m}$, whose representative material is $V_2P_2S_3Se_3$ [132].

Different classes of two-dimensional altermagnets manifest as distinct experimentally detectable features. The anomalous Hall effect (AHE) is a particularly representative case. It is well known that the AHE commonly observed in FM materials. Recently, the in-plane AHE has been investigated in two-dimensional altermagnets, featuring a coplanar alignment of the Néel vector, Hall current, and electric field [133, 134]. According to the symmetry analysis, the in-plane AHE is permitted only in d-wave altermagnets with spin Laue group ${}^{2}2/{}^{2}\mathrm{m}_x$ and in i-wave altermagnets with spin Laue group ${}^{1}\bar{3}{}^{2}\mathrm{m}$, but is strictly forbidden in the g-wave case [133]. Besides, the GMR originated from the anisotropic spin-dependent conductivities and spin-momentum coupling. Therefore, it is allowed only in d-wave altermagnets with low symmetry, whereas it is forbidden in the higher-symmetry g- and i-wave altermagnets [25].

2.3. The valley physics in altermagnets

Altermagnets, owing to their unique properties, also exhibit broad application prospects in the field of valley physics. Compared with ferromagnetic ferrovalleys, altermagnetic ferrovalleys exhibit greater advantages for valleytronic devices, including high storage density, ultrafast writing speed, and robustness against external magnetic fields owing to their zero net magnetic moment [3, 10, 135–137]. The most salient characteristic of altermagnets is their non-relativistic spin splitting [18, 19]. Usually, the valley degeneracy in altermagnets is protected by rotation symmetry $\mathcal{C}_{4z}$ and mirror symmetry $\mathcal{M}_{xy}$. Therefore, realizing valley polarization in altermagnets requires breaking these symmetries. As shown in Fig. 3, the uniaxial strain, electric field, electrostatic potential (built-in electric field), magnetic field, interlayer stacking, proximity effect and other methods can all break rotation symmetry $\mathcal{C}_{4z}$ and mirror symmetry $\mathcal{M}_{xy}$ to induce valley polarization. These approaches have been demonstrated in systems including V_2SeTeO [138, 139], $Fe_2WS_2Se_2$ [140], $Ca(CoN)_2$

[141–143], Ti_2Se_2S [144, 145], Cr_2SO [146, 147], $VPSe_3$ [132, 148], $MnPTe_3$ [149], Fe_2Se_2O [150], and so on.

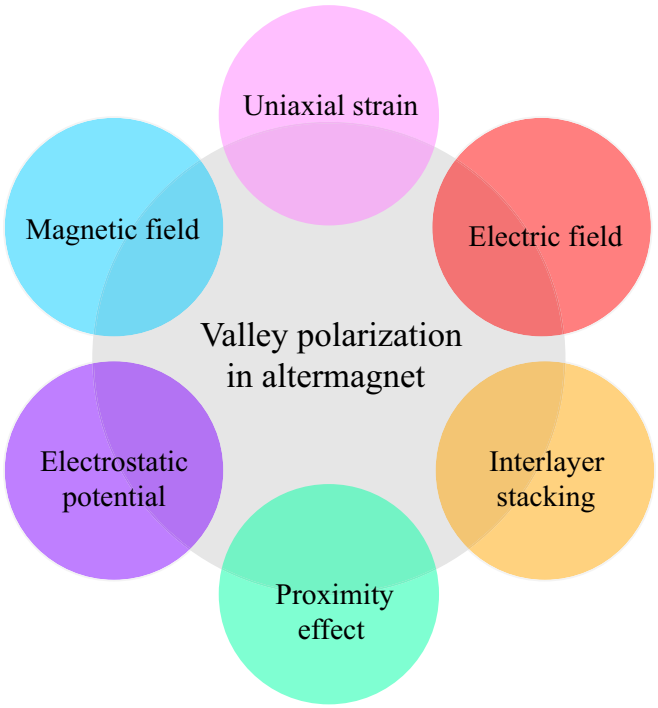


FIG. 3. The ways to achieve valley polarization in altermagnets by manipulating multiple physical fields, such as the uniaxial strain, electric field, electrostatic potential (built-in electric field), magnetic field, interlayer stacking, and proximity effect.

Moreover, altermagnets exhibit unique spin-valley locking through crystal symmetry, which has been confirmed in the V_2Se_2O system [22]. Therefore, breaking the corresponding crystal symmetry alone provides access to both spin and valley. The most representative approach is to break the mirror $\mathcal{M}_{xy}$ via uniaxial strain, inducing significant valley polarization and net magnetic moment. Simultaneously, a charge current can be applied to generate a large noncollinear spin current. This enables an effective combination of versatile spin and valley manipulation with nonvolatile information storage, which is of great significance for fundamental research and device applications in diverse fields. Recently, this effect has also been demonstrated in Fe_2Se_2O [150], $Rb_{1-\delta}V_2Te_2O$ [151], and Fe_2MoX_4 (X= S, Se, Te) [152].

3. VALLEY POLARIZATION CLASSIFICATION

Following the discovery of spontaneous valley polarization in the ferromagnetic material VSe_2 by Duan *et al.*, and the proposal of the concept of ferrovalley [86]. Spontaneous valley-polarized materials have been extensively investigate. Here, based on the symmetry that protects valley degeneracy, we classify valley polarization into three major categories. The first category consists of magnetic systems that break the $\mathcal{T}$ symmetry [86–104], termed type I valley polarization. The second category, whose valley degeneracy is protected by the $\mathcal{P}$ symmetry, realizes valley polarization mainly through the breaking of $\mathcal{P}$ symmetry by ferroelectric polarization [153, 154]. The type III spontaneous valley polarization is mainly achieved by breaking lattice symmetries, including mirror symmetry and rotational symmetry [115, 138–145, 147–150, 155, 156]. These candidate materials are summarized in Table I. Moreover, we listed the relevant symmetries in Table II for type III valley polarization.

3.1. Type I valley polarization: magnetic materials with the broken time-reversal symmetry

As a result of broken the $\mathcal{T}$ symmetry, type I ferrovalley materials have been identified in over 40 different material systems, such as ScX_2(X = Cl, Br, I) [157–159], VX_2(X = S, Se, Te) [86, 164–166], VSi_2X_4(X = N, P) [171–173], $MnPX_3$(X = S, Se, Te) [107, 108, 177], FeX_2(X = Cl, Br) [90, 91], YX_2(X = Cl, Br, I) [99], NbX_2(X = S, Se, Te) [185, 186], RuX_2(X = Cl, Br) [113, 190, 191], LuX_2(X = Cl, Br, I) [196], OsX_2(X = Cl, Br) [113, 200], LaX_2(X = Cl, Br, I) [87, 89, 202, 203], CeX_2(X = F, Cl, Br, I) [111, 204], PrX_2(X = Br, I) [203, 207], SmX_2(X = Cl, Br, I) [208], GdX_2(X = F, Cl, Br, I) [102–104, 209], and so on. Notably, valley polarization can be coupled with the quantum anomalous Hall effect [190, 191, 194]. Here, we use GdI_2 as an illustrative example [104].

As shown in Fig. 4(a), monolayer GdI_2 has a three-atomic-layer structure similar to that of 2H-phase MoS_2, where a Gd atomic layer is sandwiched between two I atomic layers. Moreover, Fig. 4(b) exhibits the typical characteristics of ionic bonding. Given that the Gd atoms in GdI_2 possess a $4f^5d^1$ electronic configuration, it follows from the Pauli exclusion principle and Hund's rule that the f and d_{z^2} orbitals are half-filled. Fig. 4(c) shows the schematic illustrations of the Gd-5d and Gd-4f orbital splitting in the trigonal-prismatic crystal field. Based on the energy minimization principle of electron hopping, monolayer GdI_2 is beneficial to the FM ground state. Intrinsic ferromagnetism breaks the $\mathcal{T}$ symmetry, thereby satisfying the symmetry requirements for type I spontaneous valley polarization. As shown in Fig. 4(d), monolayer GdI_2 is an indirect semiconductor without SOC. The valence band maximum (VBM) arises from the spin-up band at the K and K' points, while the conduction band minimum (CBM) originates from the spin-down band at the Γ point. It should be noted that the K and K' valleys of the VBM are degenerate in energy. When SOC is considered, as shown in Fig. 4(e, f), the degeneracy between the K and K' valleys is lifted (the K valley is higher in energy than the K' valley). Consequently, a spontaneous valley polarization of 155.5 meV valley splitting is generated in monolayer GdI_2. More interestingly, the valley polarization can be effectively modulated by

switching the magnetization direction from +z to -z (see Fig. 4(g)).

To reveal the underlying microscopic mechanism governing the valley splitting of the valence bands, as shown in Fig. 4(e), we first calculated the orbital-resolved band structure. The VBM mainly arises from Gd d_{xy} and $d_{x^2-y^2}$ orbitals, whereas the CBM originates from Gd d_{xy}, $d_{x^2-y^2}$ and d_{z^2} orbitals. Therefore, we used the $|\psi_v{}^\tau\rangle=\frac{1}{\sqrt{2}}(|d_{xy}\rangle+i\tau|d_{x^2-y^2}\rangle)\otimes|\uparrow\rangle$ as the orbital basis functions to build effective Hamiltonian model that describes the origin of valley polarization. The SOC effect is considered as a perturbation term,

$$\hat{H}_{SOC} = \lambda \hat{L}\cdot\hat{S} = \hat{H}^0_{SOC} + \hat{H}^1_{SOC}, \tag{1}$$

where the λ, $\hat{L}$, and $\hat{S}$ are SOC coefficient, orbital angular, and spin angular operators, respectively. $\hat{H}^0_{SOC}$ describes the interaction within the same spin states, whereas $\hat{H}^1_{SOC}$ denotes the interaction between opposite spin states. Here, we can neglect the $\hat{H}^1_{SOC}$ term, since the VBM is entirely from the spin-up band. Besides, the $\hat{H}^0_{SOC}$ can be expressed in terms of the polar angles

$$\hat{H}^0_{SOC} = \lambda\hat{S}_{z'}(\hat{L}_z cos\theta + \frac{1}{2}\hat{L}_+ e^{-i\phi} sin\theta + \frac{1}{2}\hat{L}_- e^{+i\phi} sin\theta). \tag{2}$$

When the magnetization direction of GdI_2 monolayer is along the z-axis, i.e., $\theta = \phi = 0°$. Consequently, the $\hat{H}^0_{SOC}$ term can be reduced to

$$\hat{H}^0_{SOC} = \lambda\hat{S}_z\hat{L}_z. \tag{3}$$

The VBM energy level at the K and K' valleys is defined as $E_v{}^\tau = \langle\ \psi_v{}^\tau\ |\ \hat{H}^0_{SOC}\ |\ \psi_v{}^\tau\ \rangle$. Therefore, the valley splitting can be represented as

$$E^K_v - E^{K'}_v = i\langle d_{xy}|\hat{H}^0_{SOC}|d_{x^2-y^2}\rangle - i\langle d_{x^2-y^2}|\hat{H}^0_{SOC}|d_{xy}\rangle \approx 4\beta, \tag{4}$$

where the $\hat{L}_z|d_{xy}\rangle$ = -2i$\hbar|d_{x^2-y^2}\rangle$, $\hat{L}_z|d_{x^2-y^2}\rangle = 2i\hbar|d_{xy}\rangle$, and $\beta = \lambda\langle d_{x^2-y^2}|\hat{S}_{z'}|d_{x^2-y^2}\rangle$. The analytical result demonstrates that the valence-band valley splitting is in agreement with our DFT results.

When type-I valley polarized monolayers are stacked into a bilayer, rich physical phenomena emerge. Here, we still adopt GdI_2 as an example for introduction [104]. The most intriguing phenomenon is the emergence of sliding ferroelectricity arising from interlayer stacking. Therefore, as shown in Fig. 5(a), the system realizes a two-dimensional multiferroic with simultaneous magnetic, ferroelectric, and ferrovalley properties. For the AA-stacked bilayer GdI_2, the magnetic ground state is AFM coupled. Simultaneously, the system exhibits neither spontaneous valley polarization nor ferroelectric polarization. Sliding the AA stacking configuration to AB or BA leads to a magnetic phase transition from AFM to FM, which in turn induces spontaneous valley polarization and ferroelectric polarization (depicted by dark gray arrows). Furthermore, interlayer sliding allows for the transformation between AB and BA stackings, leading to a switching of ferroelectric polarization from +z to -z axis.

As shown in Fig. 5(b), we investigate the band structures of the AA stacked bilayer GdI_2 within the AFM (M↑↓) magnetic ground state. The spin-up and spin-down bands exhibit a splitting at the VBM. At the K valley, the spin-up band is shifted upward relative to the spin-down band, while at the K' valley it is shifted downward. More strikingly, the spin-up and spin-down bands are energetically degenerate at the K and K' valleys. It is worth noting that the Berry curvatures at the K and K' valleys are of equal magnitude and opposite sign (see Fig. 5(c)). When the AA stacking shifts to AB stacking, the magnetic ground state is changed from AFM to FM. As shown in Fig. 5(d), it induces a valley polarization of 158 meV. It indicates that interlayer sliding not only induces out-of-plane ferroelectric polarization but also gives rise to the magnetic phase transition and valley polarization simultaneously. Owing to the generation of valley polarization (see Fig. 5(e)), the Berry curvatures at the K and K' valleys are no longer equal in magnitude, although their signs remain opposite. Further sliding to BA stacking causes the valley polarization to be reversed via ferroelectric switching, as illustrated in Fig. 5(f). Simultaneously, the magnitudes of the Berry curvature at the K and K' valleys are also switched (see Fig. 5(g)). Moreover, an applied electric field intrinsically breaks $\mathcal{P}$ symmetry to induce valley splitting for the centrosymmetric FM $FeCl_2$, which is still classified as type I valley polarization [222]. This will provide a theoretical basis for information storage based on valley degrees of freedom.

3.2. Type II valley polarization: ferroelectric materials with the broken spatial inversion symmetry

Type II spontaneous valley polarization arises from ferroelectric polarization that breaks the $\mathcal{P}$ symmetry. Studies on this class of materials are sparse. Currently, only two materials have been predicted, namely PbO and GeSe [153, 154]. Here, we will provide a systematic introduction using PbO as an example. For a square lattice monolayer PbO, as shown in Fig. 6(a), ferroelectric polarization is generated by atomic displacement along the x or y direction. These phases are denoted as x-FE and y-FE, respectively. In general, the valleys of this class of materials are distributed along the Γ→X and Γ→Y high symmetric paths (see Fig. 6(b)), whereas type I valleys are predominantly found at the K and K' points. In contrast to type I spontaneous valley polarization, which arises from d orbitals, this type originates from p orbital contributions. When monolayer PbO is in the paraelectric (PE) phase, as shown in Fig. 6(d), the valleys of both the VBM and CBM are degenerate. The VBM mainly originates from the O-p_x (near V_X) and p_y (near V_Y) or-

TABLE I. Two-dimensional ferrovalley materials with their types, valley polarizations, corresponding K-points, lattices, and functional.

No.	Material	Type	Valley-polarization (meV)	K-point	Lattice	Functional	Ref.
1	ScX_2(X = Cl, Br, I)	I	12/50/90	K/K'	Hexagonal	PBE	[157–159]
2	$TiInX_3$(X = Se, Te)	I	74/110	K/K'	Hexagonal	PBE	[160, 161]
3	TiTeI	I	83	K/K'	Hexagonal	PBE	[162]
4	$TiVI_6$	I	22	K/K'	Hexagonal	PBE	[163]
5	VX_2(X = S, Se, Te)	I	60/100/156	K/K'	Hexagonal	HSE/PBE/PBE	[86, 164–166]
6	VSSe	I	80	K/K'	Hexagonal	PBE	[167–169]
7	VClBr	I	70	K/K'	Hexagonal	PBE	[170]
8	VSi_2X_4(X = N, P)	I	63/49	K/K'	Hexagonal	PBE	[171–174]
9	$VSiXN_4$(X = C, Ge, Sn)	I	47/70/69	K/K'	Hexagonal	PBE	[97, 175]
10	Cr_2Se_3	I	19	K/K'	Hexagonal	PBE	[176]
11	Cr_2COOH	I	93	K/K'	Hexagonal	PBE	[112]
12	$MnPX_3$(X = S, Se, Te)	I	63/45/180	K/K'	Hexagonal	PBE	[107, 108, 177]
13	$Mn_2P_2X_3Y_3$(X ≠ Y = S, Se, Te)	I	21/98/114	K/K'	Hexagonal	PBE	[178, 179]
14	FeX_2(X = Cl, Br)	I	105/123	K/K'	Hexagonal	PBE	[90, 91]
15	FeXY(X ≠ Y = Cl, Br, I)	I	116/131/126	K/K'	Hexagonal	PBE	[92, 180]
16	$Fe(OH)_2$	I	67	K/K'	Hexagonal	PBE	[181]
17	Fe_2CFCl	I	95	K/K'	Hexagonal	PBE	[182]
18	YX_2(X = Cl, Br, I)	I	22/58/109	K/K'	Hexagonal	PBE	[99]
19	YBrI	I	82	K/K'	Hexagonal	PBE	[183]
20	ZrTeI	I	141	K/K'	Hexagonal	PBE	[184]
21	Nb_3I_8	I	107	K/K'	Hexagonal	PBE	[105]
22	NbX_2(X = S, Se, Te)	I	156/219/274	K/K'	Hexagonal	PBE	[185, 186]
23	NbN_2H_2	I	110	K/K'	Hexagonal	PBE	[187]
24	MoNX(X = Cl, Br)	I	159/151	K/K'	Hexagonal	PBE	[188]
25	$TcIrGe_2S_6$	I	161	K/K'	Hexagonal	PBE	[189]
26	RuX_2(X = Cl, Br)	I	240/354	K/K'	Hexagonal	PBE	[113, 190, 191]
27	RuClBr	I	247	K/K'	Hexagonal	PBE	[192, 193]
28	RuOHF	I	244	K/K'	Hexagonal	PBE	[194]
29	$Lu_3N_2O_2$	I	81	K/K'	Hexagonal	PBE	[195]
30	LuX_2(X = Cl, Br, I)	I	55/93/148	K/K'	Hexagonal	PBE	[196]
31	Ta_3I_8	I	200	K/K'	Hexagonal	PBE	[197]
32	TaNF	I	370	K/K'	Hexagonal	PBE	[198]
33	WNX(X = Br, Cl)	I	504/521	K/K'	Hexagonal	PBE	[199]
34	OsX_2(X = Cl, Br)	I	161/530	K/K'	Hexagonal	PBE/HSE	[113, 200]
35	OsClBr	I	150	K/K'	Hexagonal	PBE	[193, 201]
36	LaX_2(X = Cl, Br, I)	I	59/33/28	K/K'	Hexagonal	PBE/HSE/SCAN	[87, 89, 202, 203]
37	LaBrI	I	59	K/K'	Hexagonal	HSE	[88]
38	CeX_2(X = F, Cl, Br, I)	I	59/2/32/208	K/K'	Hexagonal	PBE	[111, 204]
39	CeXY(X ≠ Y = Cl, Br, I)	I	29/62/80	K/K'	Hexagonal	PBE	[205, 206]
40	PrX_2(X = Br, I)	I	55/35	K/K'	Hexagonal	PBE/SCAN	[203, 207]
41	SmX_2(X = Cl, Br, I)	I	22/62/123	K/K'	Hexagonal	PBE	[208]
42	GdX_2(X = F, Cl, Br, I)	I	55/38/82/149	K/K'	Hexagonal	PBE	[102–104, 209]
43	GdXY(X ≠ Y = Cl, Br, I)	I	63/99/117	K/K'	Hexagonal	PBE	[210]
44	TbXH(X = Br, Cl, I)	I	126/112/85	K/K'	Hexagonal	PBE	[211]
45	GeSe	II	530	V/V'	Orthorhombic	PBE	[153]
46	PbO	II	116	V/V'	Orthorhombic	PBE	[154]
47	Ti_2Se_2S	III	500	X/Y	Tetragonal	PBE	[144]
48	V_2X_2O(X = S, Se, Te)	III	60/150/170	X/Y	Tetragonal	PBE	[22, 212]
49	V_2XYO(X ≠ Y = S, Se, Te)	III	30/120/150	X/Y	Tetragonal	PBE	[138, 212]
50	$V_2P_2S_3Se_3$	III	16	K/K'	Hexagonal	PBE	[132]
51	Cr_2S_2	III	178	X/Y	Tetragonal	PBE	[213]
52	Cr_2XO(X = S, Se)	III	70/90	X/Y	Tetragonal	PBE	[146, 214]
53	Fe_2Se_2O	III	114	X/Y	Tetragonal	PBE	[150]
54	Fe_2MoX_4(X = S, Se, Te)	III	12/21/29	X/Y	Tetragonal	PBE	[152]
55	$Fe_2MoS_2X_2$(X = Se, Te)	III	74/89	X/Y	Tetragonal	PBE	[215, 216]
56	Fe_2WX_4(X = S, Se, Te)	III	11/20/42	X/Y	Tetragonal	PBE	[152, 217, 218]
57	$Fe_2WS_2Se_2$	III	11	X/Y	Tetragonal	PBE	[140, 218]
58	$Ca(CoN)_2$	III	230	X/Y	Tetragonal	PBE	[142]
59	Nb_2Se_2O	III	280	X/Y	Tetragonal	PBE	[219]
60	Nb_2SeTeO	III	260	X/Y	Tetragonal	PBE	[219, 220]
61	Nb_2Cl_2	III	112	X/Y	Tetragonal	PBE	[221]
62	$RhCl_3$	III	39	M1/M2/M3	Hexagonal	PBE	[155]
63	1T-$OsBr_2$	III	74	R1/R2/R3	Hexagonal	PBE	[115]

TABLE II. The symmetry operations protecting type III valley degeneracy and the methods to lift this degeneracy.

No.	Materials	Protected symmetry	Broken symmetry	Broken method
1	Ti_2Se_2S	$\mathcal{M}_{xy}$	$\mathcal{M}_{xy}$	uniaxial strain
2	V_2X_2O(X = S, Se, Te)	$\mathcal{M}_{xy}$	$\mathcal{M}_{xy}$	uniaxial strain
3	V_2XYO(X ≠ Y = S, Se, Te)	$\mathcal{M}_{xy}$	$\mathcal{M}_{xy}$	uniaxial strain
4	$V_2P_2S_3Se_3$	$\mathcal{PT}$	$\mathcal{PT}$	polarization
5	Cr_2S_2	$\mathcal{M}_{xy}$	$\mathcal{M}_{xy}$	uniaxial strain
6	Cr_2XO(X = S, Se)	$\mathcal{M}_{xy}$	$\mathcal{M}_{xy}$	uniaxial strain
7	Fe_2Se_2O	$\mathcal{M}_{xy}$	$\mathcal{M}_{xy}$	uniaxial strain
8	Fe_2MoX_4(X = S, Se, Te)	$\mathcal{M}_{xy}$	$\mathcal{M}_{xy}$	uniaxial strain
9	$Fe_2MoS_2X_2$(X = Se, Te)	$\mathcal{M}_{xy}$	$\mathcal{M}_{xy}$	magnetic field
10	Fe_2WX_4(X = S, Se, Te)	$\mathcal{M}_{xy}$	$\mathcal{M}_{xy}$	uniaxial strain
11	$Fe_2WS_2Se_2$	$\mathcal{M}_{xy}$	$\mathcal{M}_{xy}$	uniaxial strain
12	$Ca(CoN)_2$	$\mathcal{TS}_{4z}$	$\mathcal{TS}_{4z}$	electric field
13	Nb_2Se_2O	$\mathcal{M}_{xy}$	$\mathcal{M}_{xy}$	uniaxial strain
14	Nb_2SeTeO	$\mathcal{M}_{xy}$	$\mathcal{M}_{xy}$	uniaxial strain
15	Nb_2Cl_2	$\mathcal{M}_{xy}$	$\mathcal{M}_{xy}$	uniaxial strain
16	$RhCl_3$	$\mathcal{C}_{3z}$	$\mathcal{C}_{3z}$	interlayer stacking
17	1T-$OsBr_2$	$\mathcal{C}_{3z}$	$\mathcal{C}_{3z}$	interlayer stacking

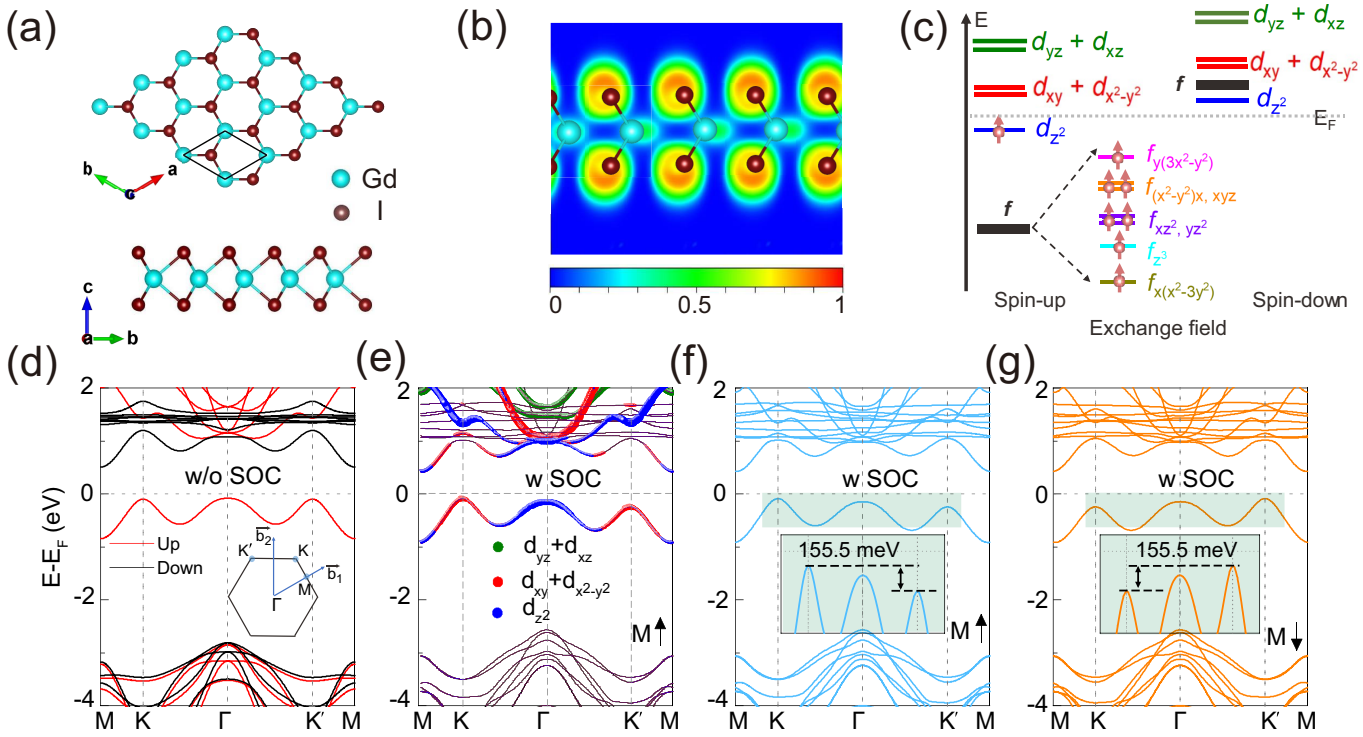


FIG. 4. (a) Top and side views of the crystal structures of monolayer GdI_2. The light blue and brown balls represent Gd and I elements, respectively. (b) Electron localization function of GdI_2. (c) Phonon spectrum of GdI_2 along high-symmetry lines. (d) Spin-polarized band structure and (e) Orbital-resolved band structure with SOC of monolayer GdI_2. (f, g) Band structures with SOC for magnetic moments along +z (f) and -z (g), respectively [104].

bitals, while the CBM mainly arises from the Pb-p_x (near V_X) and p_y (near V_Y) orbitals. Upon switching to the FE phase, the intrinsic polarization breaks $\mathcal{P}$ symmetry, which removes the valley degeneracy (see Fig. 6(c, e)). More interestingly, the reversal of ferroelectric polarization enables effective switching of the valley polarization direction.

Leveraging the valley-selective optical response to linearly polarized light, optical characterization offers a noncontact and nondestructive route to identify valley polarization and its polarity switching in type II ferrovalley materials. Since the ferrovalley state depends on the electric dipole orientation and can be switched by an external electric field, it offers a route to tune the direction

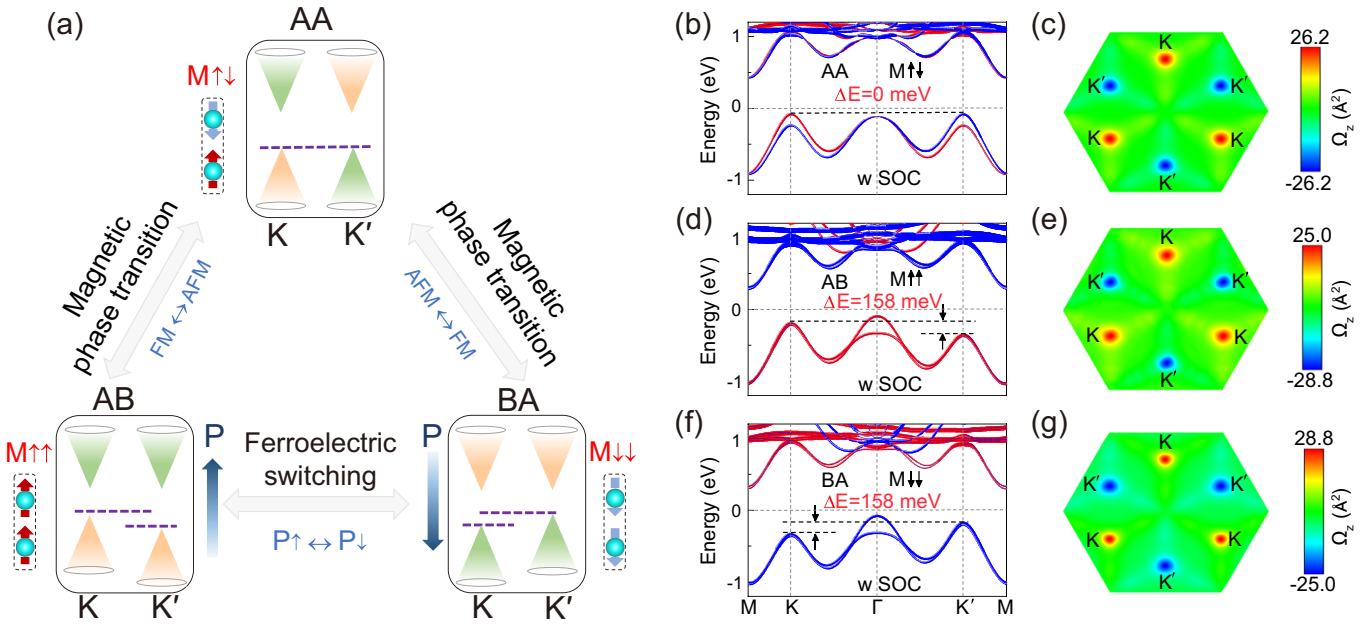


FIG. 5. (a) Mechanism of a multiferroic with coexisting magnetic, ferroelectric, and ferrovalley properties. Spin-resolved band structures and Berry curvatures of AA (b, c), AB (d, e), and BA (f, g) stacking bilayer GdI_2 under the SOC effect [104].

of linearly polarized light. Therefore, as shown in Fig. 7, Duan *et al.* proposed electrically controllable polarizer based on the type II ferrovalley materials [153]. Under an in-plane electric field along the x-direction, the band gap resides in the V_X valley, enabling electron excitation via laser absorption. In the photoluminescence process, the excited electrons at the V_X valley eventually re-emit photons when they relax back to the ground state. Upon application of the electric field along the y-axis by the double-throw switch, the transitions ferroelectricly from the x-FE to y-FE phase. Simultaneously, the sign of the valley polarization is reversed. In general, ferroelectric polarization switching typically shows ultrafast dynamics, whose time scale can range from microseconds to nanoseconds [223, 224]. Owing to the linearly polarized optical selectivity of valleys, the ferrovalley-based polarizer allows for dynamic electrical polarization of the laser beam along either x or y-direction with both high speed and improved accuracy.

Besides, when a quarter-wave plate is oriented perpendicular to the propagation of linearly polarized light, and its optical axis is set at 45° anticlockwise from the x-direction (or equivalently clockwise from the y-direction), the circular polarization chirality becomes electrically tunable in an analogous fashion. Linearly polarized light along the x-axis, emitted under an applied electric field in the same direction, undergoes a transition to left-handed radiation. By switching the direction of ferroelectric polarization, the right-handed also will be generated. The convenient manipulation of valley polarization provides a broader platform for its applications.

3.3. Type III valley polarization: materials with the broken lattice symmetry

Unlike type I and type II valley degeneracy, which are protected by $\mathcal{T}$ and P symmetries, type III valley degeneracy is protected by lattice symmetry. Such symmetries typically include mirror symmetry and rotational symmetry, among others. Therefore, such spontaneous valley polarization can occur in either magnetic or nonmagnetic systems. In the following sections, we choose representative nonmagnetic bilayer $RhCl_3$ and magnetic $Fe_2WS_2Se_2$ systems for a detailed introduction.

3.3.1. Type III valley polarization in non-magnetic materials

In 2024 year, Xiang *et al.* firstly proposed the concept of bilayer stacking ferrovalley (BSFV) [155]. Unlike existing paradigms, the BSFV method does not rely on magnetism or ferroelectricity. Consequently, it does not require breaking $\mathcal{T}$ or $\mathcal{P}$ symmetries. In essence, BSFV is achieved by using bilayer stacking to break the symmetries that couple the degenerate valleys in the monolayer Brillouin zone, as shown in Fig. 8(a, b). For the hexagonal lattice, as shown in Fig. 8(c), the degeneracy valleys are linked by $\mathcal{C}_{3z}$ rotational symmetry. However, when the symmetry is broken by bilayer stacking, valley polarization can be induced (see Fig. 8(d)).

Group theory analysis can provide a better understanding of its microscopic mechanism. G denotes the layer group of a monolayer, and one of its degenerate

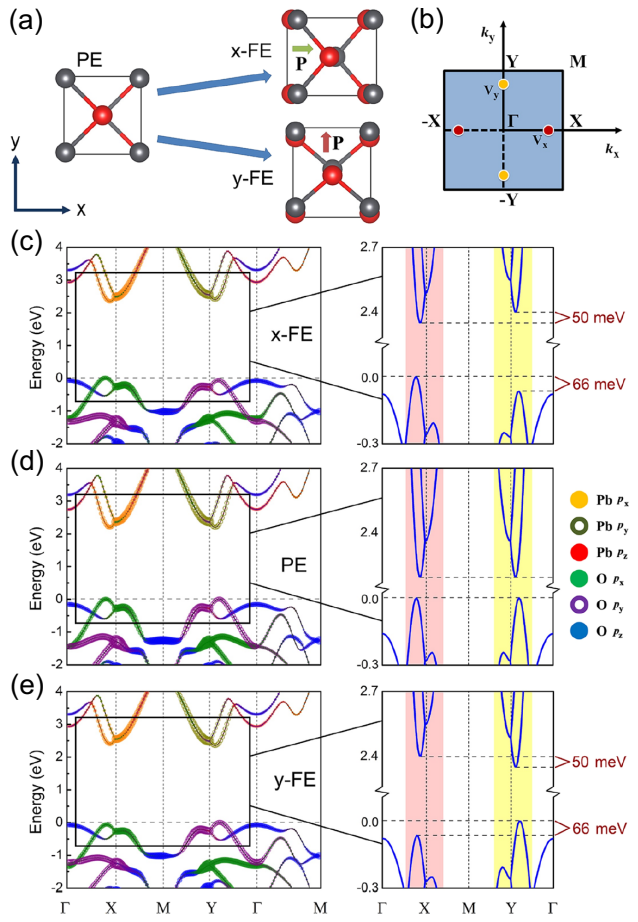


FIG. 6. (a) Schematic illustrations of monolayer PbO in the non-polar paraelectric state and ferroelectric states with polarization vectors along the x- and y-directions, respectively. The gray and red balls denote Pb and O elements respectively. (b) The two valleys in the Brillouin zone of the orthogonal lattice are marked as V_X and V_Y. (c-e) The band structures of monolayer PbO for the x-FE, PE, and y-FE phases, respectively [154].

valleys is located at $\boldsymbol{k}$. Under all operations g in G, the valley at $\boldsymbol{k}$ is either invariant or becomes degenerate valleys $\boldsymbol{k}$' = $g_c\boldsymbol{k}$. Since the energy condition $E(\boldsymbol{k}) = E(g_c\boldsymbol{k})$ holds, where g_c denotes the connecting symmetry that their aim to break. In principle, while bilayer stacking can break all point group symmetries, but it cannot break $\mathcal{T}$ symmetry. Therefore, the valley degeneracy protected by $\mathcal{T}$ symmetry between (k_x, k_y) and (-k_x, -k_y), e.g., K and K' in hexagonal lattices. They cannot cannot produce polarization by bilayer stacking. Next, we mainly explore valley degeneracy that is protected by other symmetries.

In the hexagonal lattice, the threefold rotational symmetry $\mathcal{C}_{3z}$ leads to valley degeneracy among $\boldsymbol{k}$, $\mathcal{C}_{3z}\boldsymbol{k}$, and $\mathcal{C}_{3z}\boldsymbol{k}$. Therefore, as shown in Fig. 8(c, d), the valley polarization can be induced by breaking this symmetry. Xiang *et al.* performed a data-driven screening of two-dimensional materials and discovered 352 type III non-magnetic ferrovalley materials [155]. Here, we take hexagonal $RhCl_3$ as an example. As shown in Fig. 8(e), the crystal structure of bilayer $RhCl_3$ features a honeycomb lattice of edge-sharing octahedra, analogous to that of CrI_3. As shown in Fig. 8(f), sliding by D_1 (1/3, 2/3) and D_2 (2/3, 1/3) gives rise to an energy doublet corresponding to the global minima, while sliding by L_1 (1/3, 0), L_2 (0, 1/3), and L_3 (2/3, 2/3) results in a triplet that are local minima. In the G stacking configuration, the valleys are degenerate at the M_1, M_2, and M_3 points, as illustrated in Fig. 8(g). When sliding to the L_1 stacking, as shown in Fig. 8(h), the energy degeneracy at M_1, M_2, and M_3 points is broken, making the valley at M_2 different from those at M_1 and M_3. Moreover, we have verified this mechanism in bilayer 1T-phase $OsBr_2$ [115]. And a triple valley polarized state was achieved.

3.3.2. Type III valley polarization in magnetic materials

As valley polarization can be induced in non-magnetic systems by breaking the lattice symmetry, it is natural to question whether magnetic systems exhibit similar behavior. The answer is in the affirmative. In the monolayer non-Janus $Fe_2WS_2Se_2$, we also found evidence of type III valley polarization [140].

The crystal structure of monolayer non-Janus $Fe_2WS_2Se_2$ is shown in Fig. 9(a, b). They are composed of three atomic layers, with an Fe-W atomic layer sandwiched between two S-Se atomic layers. Furthermore, the S and Se atoms are arranged in columns, with Fe or Fe-W separating rows between them. Its space group is P2. Therefore, there is no symmetry operation linking the two sublattices in non-Janus $Fe_2WS_2Se_2$. Therefore, it is full compensated ferromagnetism. This constitutes the most significant distinction from other altermagnets, and also serves as the key to realizing type III spontaneous valley polarization. Besides, it exhibits $\mathcal{C}_{2y}$ rotation symmetry. The low structural symmetry gives rise to its novel magnetic anisotropy energy (MAE). Hence, we systematically investigate the magnetic anisotropy distribution across the entire space. As shown in Fig. 9(c-e), the xz and yz planes show typical uniaxial magnetic anisotropy. It is well described by the equation

$$\mathrm{MAE} = \mathrm{K}_1\cos^2\theta + \mathrm{K}_2\cos^4\theta. \tag{5}$$

It is worth noting that the xy plane is entirely beyond the description of Eq. (5). It displays an unusual four-leaf-clover pattern, indicative of biaxial MAE. It is necessary to write its Hamiltonian in a fourth-order expansion [140, 225]

$$H_{\mathrm{MAE}} = \sum_i A_4(S_{ix}^2S_{iy}^2 + S_{ix}^2S_{iz}^2 + S_{iy}^2S_{iz}^2), \tag{6}$$

where A_4 represents the fourth-order single-ion anisotropy. As shown in Fig. 9(c), the four degen-

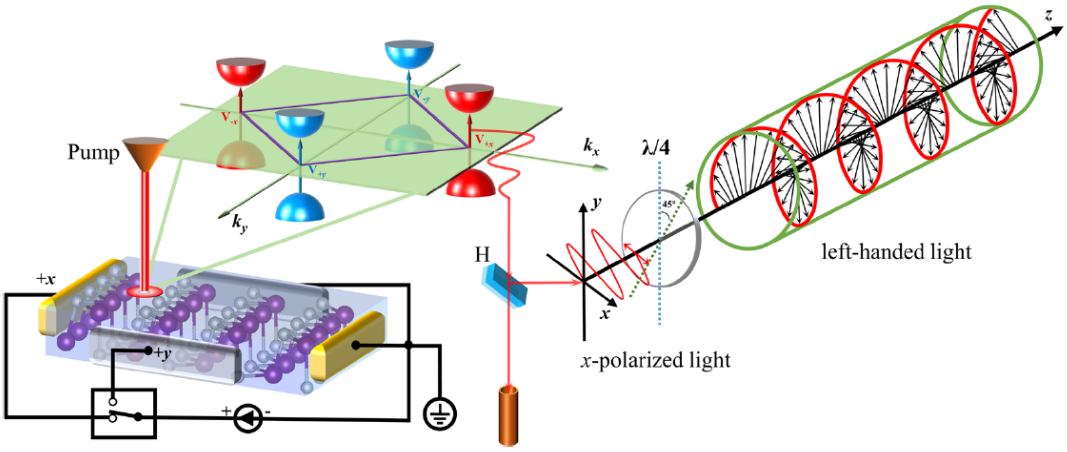


FIG. 7. Electrically tunable polarizer based on the type II ferrovalley materials [153].

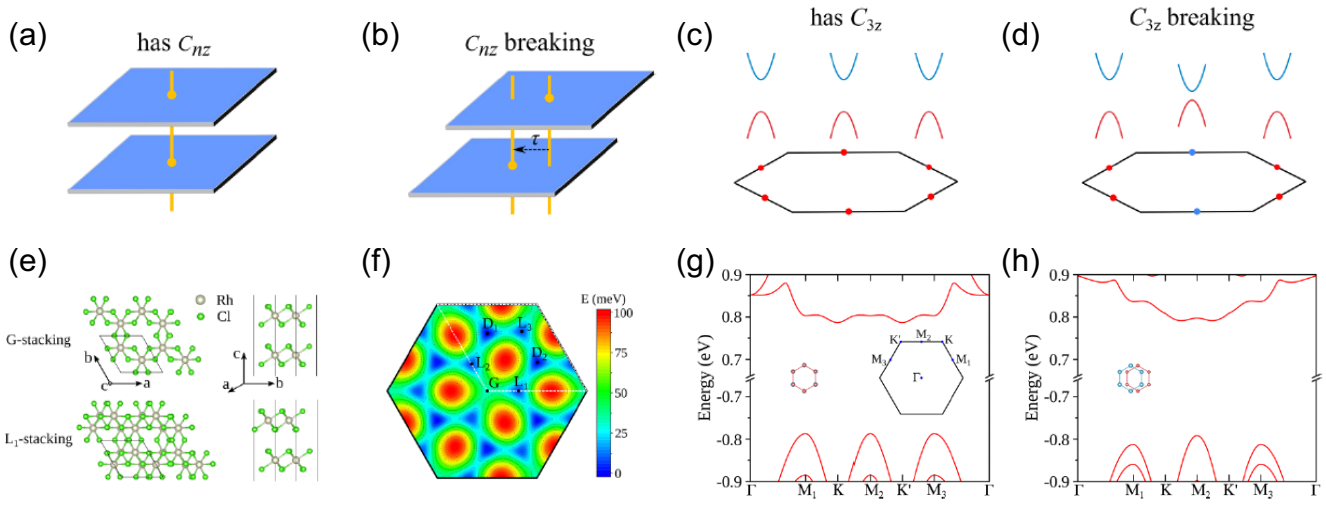


FIG. 8. Schematic illustrations of (a) a bilayer with $\mathcal{C}_{nz}$ rotational symmetry and (b) the breaking of $\mathcal{C}_{nz}$ symmetry induced by interlayer sliding τ. (c) Brillouin zone of a hexagonal lattice, with degenerate valleys linked by $\mathcal{C}_{3z}$ symmetry. (d) Valley polarization induced by the breaking of $\mathcal{C}_{3z}$ symmetry through interlayer sliding. The degenerate and polarized valleys are denoted by red and blue dots, respectively. (e) The top and side views of the G and L_1 stackings bilayer $RhCl_3$. The silver and green balls denote Rh and Cl elements respectively. (f) Energy landscapes of various bilayer stacking configurations. The band structures of G (g) and (h) L_1 stackings without SOC [155].

erate energy minima are located along the [110] and [1$\bar{1}$0] directions. More interestingly, the orientation of the four degenerate energy minima is solely determined by the atomic positions of S and Se. The S and Se atoms of non-Janus $Fe_2WS_2Se_2$ are distributed in the horizontal direction. Therefore, it shows a four-leaf-clover pattern aligned parallel to the x and y axes. This has significant potential in spin-based storage applications, where the biaxial MAE can be utilized to store higher-order logic bits in biaxial magnetic tunnel junctions.

To substantiate that the spontaneous valley polarization arises from the breaking of lattice symmetry, we performed calculations of the spin-polarized band structures. As shown in Fig. 9(f), it is a direct band gap semiconductor, whose VBM and CBM lie at the X and Y points. The VBM and CBM at the X point are spin-down bands, while those at the Y point are spin-up bands. We have proven theoretically that the VBM and CBM at the X and Y points are degenerate in energy when the system has $[\mathcal{C}_2\|\mathcal{M}_{xy}]$ symmetry [140]. However, the $[\mathcal{C}_2\|\mathcal{M}_{xy}]$ symmetry is broken in non-Janus $Fe_2WS_2Se_2$. Therefore, the energy degeneracy at the X and Y points is lifted, resulting in valley splittings of 2.27 meV for the VBM and 8.40 meV for the CBM (see Fig. 9(f)). This

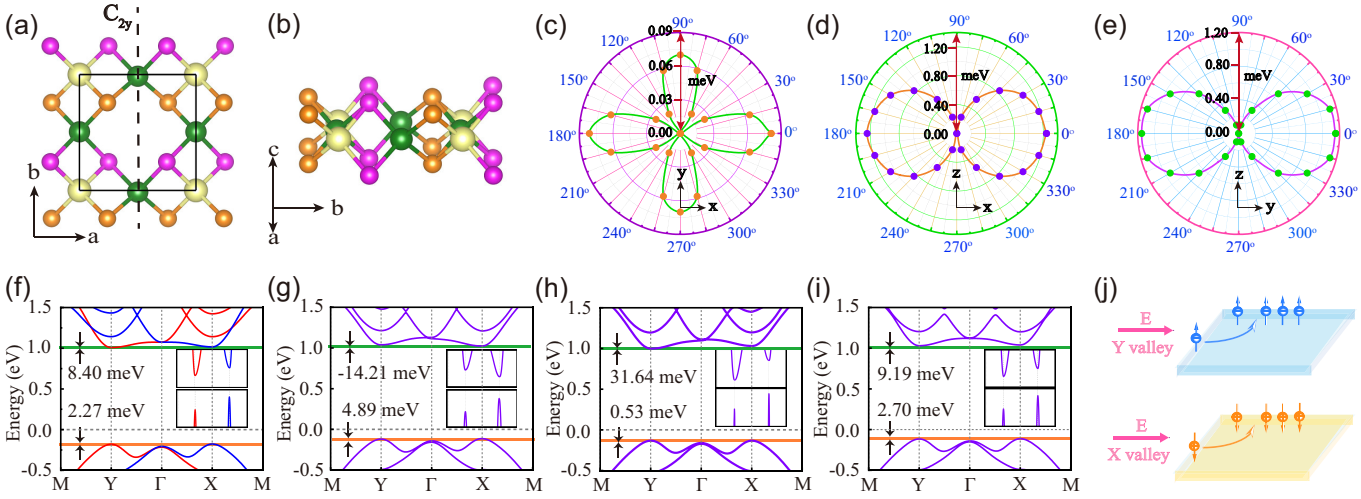


FIG. 9. (a, b) Crystal structures of monolayer non-Janus $Fe_2WS_2Se_2$ in the top and side views. The green, light yellow, orange, and magenta balls show Fe, W, S, and Se elements respectively. (c-e) Angular dependence of the MAE for monolayer non-Janus $Fe_2WS_2Se_2$ with the magnetization direction lying in the (c) xy, (d) xz, and (e) yz planes, respectively. (f-i) Band structure of monolayer non-Janus $Fe_2WS_2Se_2$. (f) Spin-polarized band structures, (g) with the M//x SOC effect, (h) with the M//y SOC effect, and (i) with the M//z SOC effect. (j) Schematic illustration of the anomalous valley Hall effect [140].

finding further corroborates that type III spontaneous valley polarization can be realized in magnetic systems by breaking the lattice symmetry. In addition, as shown in Fig. 9(g-i), the valley polarization is significantly influenced when SOC is taken into account. Valley splitting is present for each of the +x, +y, and +z magnetization directions. In contrast to hexagonal lattices, valley polarization usually arises when the magnetization is oriented out of the plane [86, 87, 89–92]. The orbital composition results in a greater valley splitting for the CBM than for the VBM. As shown in Fig. 9(g, h), valley splitting exhibits completely different behavior for magnetizations along the x-axis and y-axis. For magnetization along x, the valley splitting of VBM and CBM is markedly enhanced, while the valley polarization direction of CBM is also switched. When the magnetization direction is switched to the y-axis, the valley splitting of the VBM decreases. It is noteworthy that the CBM valley polarization undergoes both a sign reversal and an enhancement in magnitude. As shown in Fig. 9(i), when the magnetization is along the z-axis, the valley splitting magnitude is nearly identical to that in the absence of SOC. The pronounced variation of valley splitting with magnetization direction is highly relevant for the device applications of valleytronics.

A thorough understanding of the microscopic mechanism underlying the anomalous valley Hall effect (AVHE) is of paramount importance for valleytronic device applications. Hence, as shown in Fig. 9(j), we designed a schematic diagram of the AVHE for non-Janus $Fe_2WS_2Se_2$. When the Fermi level is set between the X and Y CBM valleys, as shown in the upper pane of Fig. 9(j), spin-up electrons from Y accumulate on the left edge of non-Janus $Fe_2WS_2Se_2$ under an in-plane field. This shift of the Fermi level between the X and Y VBM valleys results in a left-side accumulation of spin-down holes (see the lower panel of Fig. 9(j)). The abundant AVHE opens up more avenues for valleytronics. Moreover, the valley splitting of hidden altermagnet Cr_2SO originates from the in-plane magnetization breaking the $\mathcal{C}_{4z}\mathcal{T}$ or $\mathcal{M}_{xy}\mathcal{T}$ symmetries [226]. Therefore, it belongs to type III valley polarization. Until now, VS_2 [227], VSe_2 [228], Cr_2Se_3 [229], $MnPS_3$ [230], $NbSe_2$ [231], GeSe [232], and V_2Se_2O [233] have been successfully prepared.

4. MULTIFIELD TUNABLE VALLEY POLARIZATION IN ALTERMAGNETS

In altermagnets, the valley serves as a representative order parameter, giving rise to non-relativistic valley polarization that is independent of SOC. This phenomenon originates from the breaking of lattice symmetry, which is fundamentally different from the conventional SOC-induced breaking of the $\mathcal{T}$ symmetry. Therefore, it can also be categorized as type III valley polarization. The discovery of novel valley polarization in altermagnets has significantly advanced the field of valleytronics. Regulating valley polarization in altermagnets is essential for the application of valleytronics in information storage. In the following, we will provide a detailed discussion on the multiphysical regulation of valley polarization by strain, electric field, magnetic field, interlayer stacking, proximity effect, and so on, and also examine their feasibility in device applications. We listed the tuning methods, materials, broken symmetry operations protecting valley degeneracy, and the magnitude of valley splitting to Table III.

TABLE III. The tuning method, materials, broken symmetry operations protecting valley degeneracy, and the magnitude of valley splitting.

Tuning Method	Materials	Broken symmetry	Valley polarization (meV)
Strain	V_2SeTeO	$\mathcal{M}_{xy}$	128
	Ti_2Se_2S	$\mathcal{M}_{xy}$	600
	Cr_2SO	$\mathcal{M}_{xy}$	48
	Fe_2Se_2O	$\mathcal{M}_{xy}$	114
	Nb_2Se_2O	$\mathcal{M}_{xy}$	264
	Mo_2Te_2O	$\mathcal{M}_{xy}$	84
Electric field	V_2Se_2O	$\mathcal{M}_{xy}$	147
	$VPSe_3$	$\mathcal{M}_{xy}$	3
Electrostatic potential	$V_2P_2S_3Se_3$	$\mathcal{PT}$	16
	$Mn_2P_2S_3Te_3$	$\mathcal{M}_{xy}$	39
Magnetic field	$Fe_2MoS_2Se_2$	$\mathcal{M}_{xy}$	2
	$Fe_2WS_2Se_2$	$\mathcal{M}_{xy}$	24
	Mo_2Te_2O	$\mathcal{M}_{xy}$	17
Interlayer stacking	Fe_2MoS_4	$\mathcal{M}_{xy}$	7
	$Ca(CoN)_2$	$\mathcal{TS}_{4z}$	29
	Cr_2WS_4	$\mathcal{M}_{xy}$	86
	MOF	$\mathcal{S}_4$	201
Proximity effect	V_2Se_2O/SnO	$\mathcal{M}_{xy}$	379
	V_2S_2O/CrP	$\mathcal{M}_{xy}$	537
	$Ca(CoN)_2/CoX$ (X = Cl_2, Se)	$\mathcal{TS}_{4z}$	306/709

4.1. Strain tunable valley polarization

Two-dimensional materials exhibit a high sensitivity of their physical properties, such as the magnetic ground state, electronic structure, and topological properties, to strain-induced lattice deformation. Interestingly, the valley polarization in altermagnets originates from lattice symmetry breaking, making it effectively tunable by strain. In 2024, Zhu *et al.* revealed that the valley in V_2SeTeO is protected by the mirror symmetry $\mathcal{M}_\Phi$ [138]. As shown in Fig. 10(a), the substitution of Se by Te in the bottom layer of V_2Se_2O gives rise to the Janus monolayer V_2SeTeO [22]. It has lower symmetry because the out-of-plane mirror symmetry is broken, while the tetragonal structure and in-plane $\mathcal{C}_4$ and $\mathcal{M}_\Phi$ symmetries are preserved. To better understand the electrical properties, the spin-polarized band structure is shown in Fig. 10(b). The Brillouin zone employed for band structure calculations is illustrated in Fig. 10(c), which corresponds to the crystal structure. It possesses a direct band gap of 0.25 eV, while also displaying spin splitting different from that of conventional antiferromagnets. This phenomenon is attributed to the altermagnetic order depicted in Fig. 10(a), which breaks the $\mathcal{PT}$ and $\mathcal{UI}$ symmetries ($\mathcal{U}$: spinor symmetry, $\mathcal{I}$: translation symmetry), thus allowing spin splitting. It is noteworthy that the valley degeneracy at the X and Y points arises from V atoms with opposite spin orientations (see Fig. 10(b)). When the SOC is included, the valley degeneracy at the X and Y points is still present.

Valley degeneracy is protected by the $\mathcal{M}_\Phi$ mirror symmetry. Consequently, uniaxial strain can break the symmetry and produce a pronounced valley polarization. This is quite akin to other piezo effects, including piezoelectricity and piezomagnetism. The relevant physical properties are mechanical responses to applied strain, such as magnetization and electric polarization. The valley polarization in altermagnets, analogous to the above effects, can be defined as the piezovalley effect. Fig. 10(d) illustrates the physical mechanism of the piezovalley. Compressive and tensile strain can effectively modulate the magnitude and direction of valley polarization, which can be utilized for valleytronic information storage. As shown in Fig. 10(e), the valley polarization exhibits a monotonic variation under strain, with opposite trends along the a and b directions, owing to the diagonal mirror symmetry $\mathcal{M}_\Phi$. These findings suggest that the predicted Janus monolayer V_2SeTeO retains its altermagnetic character and manifests a considerably enhanced piezovalley response under strain. Moreover, the strain-induced valley polarization provides new avenues for the generation of net magnetization. Strain tuning of valley polarization in altermagnets has been reported in many materials, like Ti_2Se_2S [144], Cr_2SO [146], Fe_2Se_2O [150], Nb_2Se_2O [219], and Mo_2Te_2O [234]. The piezovalley effect is anticipated to be applied in nanoelectronics, valleytronics, and spintronics.

4.2. Electric field tunable valley polarization

An electric field is one of the most efficient and reliable approaches to tuning material properties in experimental and practical settings. The major reason is the convenient application and the non-destructive nature toward the material. The essence of tuning material properties with an electric field is to modify the internal potential distribution, which enables effective manipulation of the

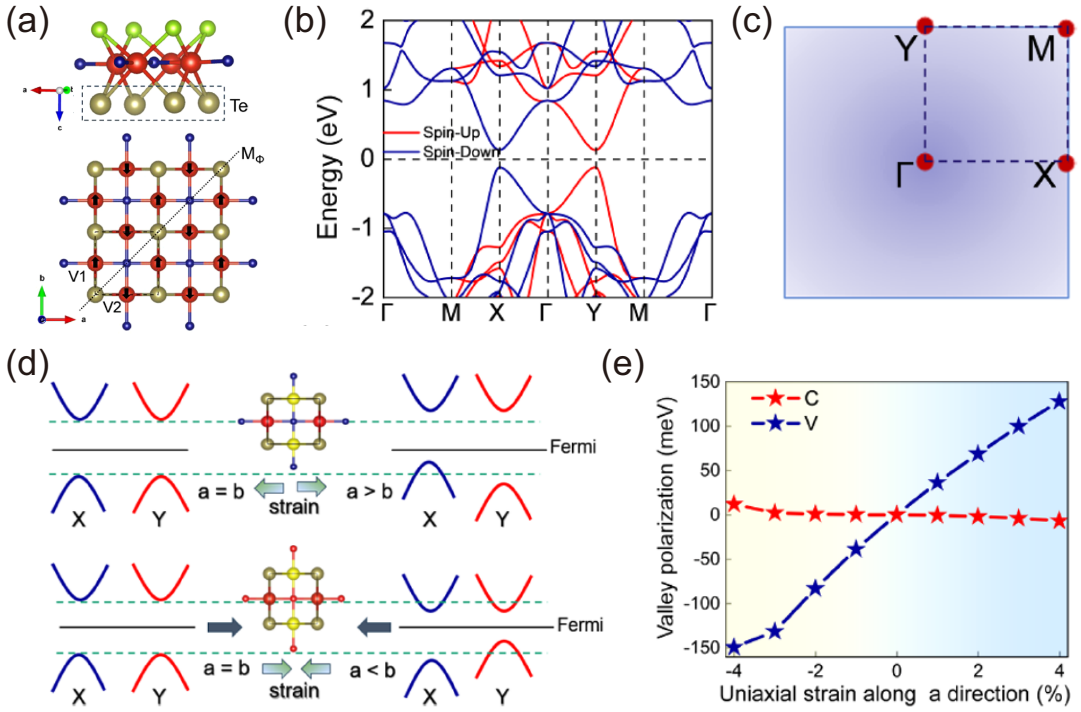


FIG. 10. (a) Crystal structures of Janus V_2SeTeO. The red, dark blue, brown and light green balls show V, O, Te, and S elements respectively. (b) Spin-resolved band structure of V_2SeTeO. (c) The first Brillouin zone with the high-symmetry points marked. (d) Schematic illustration of the piezovalley mechanism. (e) Uniaxial strain modulates the valence (V) and conduction (C) bands to generate valley polarization [138].

electronic structure, symmetry, and lattice/spin coupling effects. Here, we mainly introduce valley polarization induced by lattice symmetry breaking via in-plane and out-of-plane electric fields.

Firstly, Zhan *et al.* systematically investigated the crystal symmetry of monolayer V_2Se_2O [235]. As shown in Fig. 11(a), they found that an electric field applied along either the [100] or [010] direction simultaneously breaks the $\mathcal{C}_{2a}$, $\mathcal{C}_{2b}$, $\mathcal{M}_a$, and $\mathcal{M}_b$ symmetries, thereby preventing the interchange of the two spin sublattices. Consequently, both valley polarization and spin polarization will appear. In contrast, when the electric field is oriented parallel to the mirror planes (e.g., along [110] or [1$\bar{1}$0]), certain corresponding symmetries are preserved (see Fig. 11(a)). Therefore, the X and Y valleys remain degenerate. As shown in Fig. 10(b), when the electric field is applied along the [100] direction, both the VBM and CBM exhibit significant valley polarization. The switching of the electric field to the [010] direction results in a valley polarization of the same magnitude but opposite sign. This stems from the fact that the mirror symmetry connects the two valleys, which are occupied by different V atoms. Additionally, the valley polarization in V_2Se_2O exhibits tunability with respect to both the direction and magnitude of the applied electric field. As shown in Fig. 11(c), when the magnitude of the electric field is set to 0.15 V/Å, valley polarization exhibits a maximum for field orientation along [100] or [010] directions. The valley polarization first decreases to zero at 45° and then increases to a maximum at 90°, which exhibits a clover-like variation. Interestingly, when the electric field is aligned parallel to the $\mathcal{C}_{2a}$ or $\mathcal{C}_{2b}$ rotational axes, the valley polarization vanishes. In addition, an increase in valley splitting is observed with the increase of electric field strength along [100] and [010] (see Fig. 11(c)). On the contrary, when the electric field is applied along [110], valley polarization is absent even at high strengths, because the $\mathcal{M}_a$ and $\mathcal{C}_{2a}$ symmetries remain unbroken.

Then, we propose that an out-of-plane electric field breaks $\mathcal{PT}$ symmetry (see Fig. 11(d)), inducing a transition of monolayer $VPSe_3$ from a Neel AFM state to an altermagnetic state, thereby achieving valley polarization [132]. Although monolayer $VPSe_3$ breaks both $\mathcal{P}$ and $\mathcal{T}$ symmetries individually, it preserves the combined $\mathcal{PT}$ symmetry, which gives rise to Kramers degeneracy in its band structure. When the out-of-plane electric field is applied, this leads to inequivalence between the upper and lower Se atomic layers, which in turn breaks the $\mathcal{PT}$ symmetry. When the SOC is switched off, the band structure has $\mathcal{C}_6$ rotational symmetry. Special high-symmetry lines satisfy the relation $E(s, \text{-}\mathbf{k}) = E(\text{-}s, \text{-}\mathbf{k})$. As shown in Fig. 11(f), the valleys at the K and K' points of the CBM are completely degenerate under an out-of-plane electric field

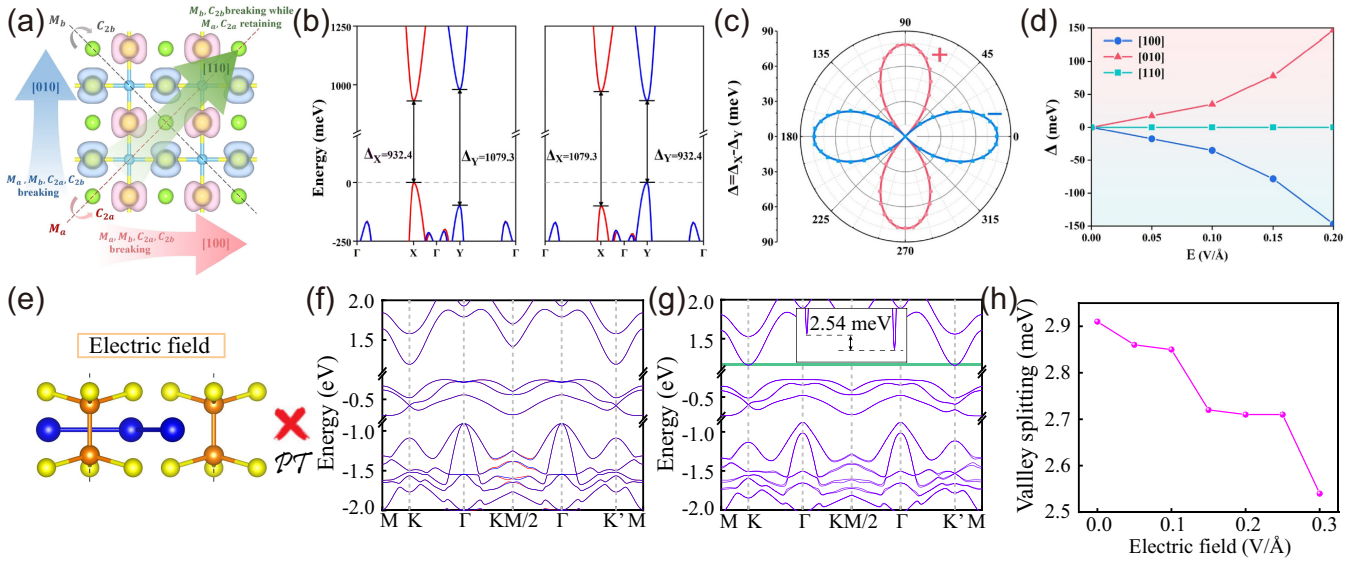


FIG. 11. (a) Schematic diagram of lattice symmetry breaking in monolayer V_2Se_2O under electric fields along different directions. The light yellow, light blue, and light green balls denote V, O, and Se elements respectively. (b) Spin-polarized band structures under a 0.2 V/Å electric field along [100] (left) and [010] (right), respectively. (c) Variation of valley splitting with angle for a 0.15 V/Å electric field. Red lines denote positive valley polarization, while blue lines denote negative ones [235]. (d) Valley polarization as a function of electric field direction along [100], [010], and [110]. (e) Schematic illustration of $\mathcal{PT}$ symmetry broken in monolayer $VPSe_3$ by an applied out-of-plane electric field. The blue, orange, and yellow balls represent V, P, and Se elements respectively. (f, g) Band structures (f) without SOC and (g) with SOC under a 0.3 V/Å electric field. (h) Valley splitting of monolayer $VPSe_3$ versus the external electric field [132].

of 0.3 V/Å. However, spin splitting is observed along the Γ-KM/2-Γ path, which is a typical characteristic of an altermagnet. When the SOC is included, the rotational symmetry of the band structure decreases from $\mathcal{C}_6$ to $\mathcal{C}_3$. Therefore, as shown in Fig. 11(g), the valley degeneracy at the K and K' points of the CBM is lifted, inducing a valley polarization of 2.54 meV. Furthermore, the valley splitting varies by only 0.4 meV from 0.0 to 0.3 V/Å (see Fig. 11(h)), which primarily originates from the non-magnetic Se atoms. An electric field can readily control both the magnitude and direction of valley polarization in altermagnets, offering a straightforward route that is crucial for information technology.

4.3. Electrostatic potential tunable valley polarization

In the previous chapter, we mentioned that the essence of an electric field is to alter the distribution of potential inside the material. Not only external electric fields but also functionalized Janus can alter the chemical potential distribution. Therefore, the $\mathcal{PT}$ symmetry will be broken. As shown in Fig. 12(a), monolayer $VPSe_3$ possesses $\mathcal{PT}$ combined symmetry. Therefore, as shown in Fig. 12(b), the spin up and spin down bands are degenerate throughout the entire Brillouin zone. When the bottom Se atoms are replaced by S atoms, a Janus structure $V_2P_2S_3Se_3$ is formed (see Fig. 12(c)). The asymmetry between the lower and upper surfaces of the Janus structure gives rise to a significant built-in electric field. This built-in electric field has an effect equivalent to that of an external electric field, thereby breaking $\mathcal{PT}$ symmetry. As shown in Fig. 12(d), this will lead to the lifting of Kramers degeneracy, manifesting the characteristic spin splitting of altermagnets. Besides, we calculated the planar averaged electrostatic potential of Janus $V_2P_2S_3Se_3$. As shown in Fig. (e), a significant potential difference between the top and bottom surfaces can be clearly observed. Here, we defined the built-in electric field as $E_{in} = (\Phi_2 - \Phi_1)/\Delta h$, where Φ_1, Φ_2, and Δh denote the electrostatic potentials at the upper and lower surfaces and the structural height of $V_2P_2S_3Se_3$, respectively. The built-in electric field of Janus $V_2P_2S_3Se_3$ is 0.10 V/Å. As shown in Fig. 12(f), the spin-polarized bands of Janus $V_2P_2S_3Se_3$ exhibit clear alternated spin splitting along the Γ-KM/2-Γ path. It is worth noting that the valleys at the K and K' points of the CBM are still degenerate. This means that it is not a lattice symmetry protected valley degeneracy. Besides, the Berry

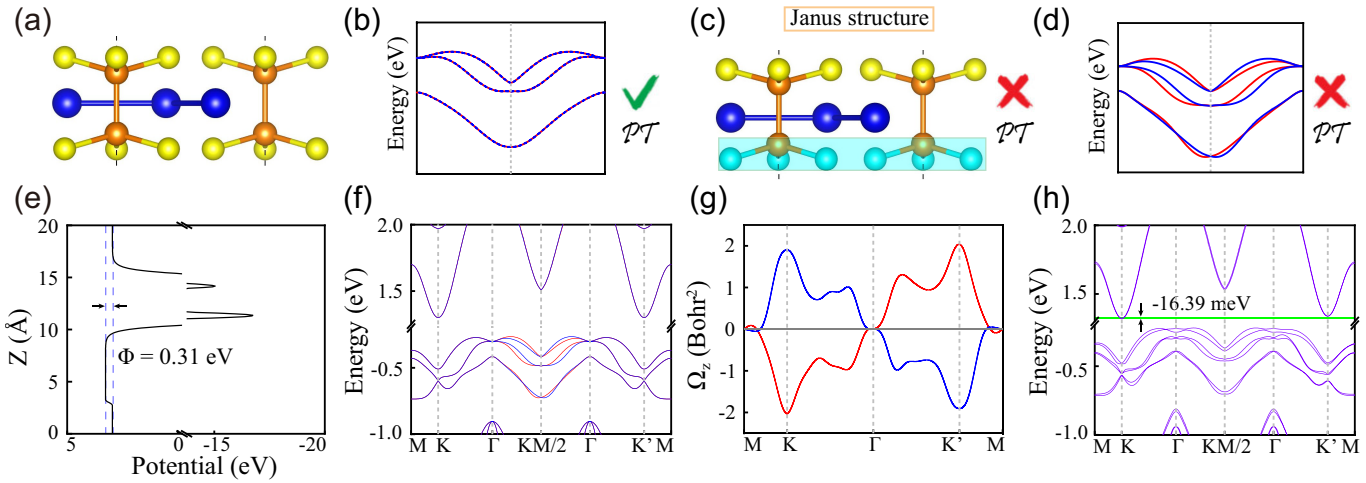


FIG. 12. (a) Crystal structure of monolayer $VPSe_3$. The blue, orange, and yellow balls represent V, P, and Se elements respectively. (b) Schematic band structure of the Neel AFM state with $\mathcal{PT}$ symmetry. (c) The crystal structure is functionalized into a Janus configuration via substitution of the bottom Se layer by S atoms. (d) Schematic band structure of the altermagnetic state with broken $\mathcal{PT}$ symmetry. (e) Planar-averaged electrostatic potential of monolayer Janus $V_2P_2S_3Se_3$. (f, h) Band structure of of monolayer Janus $V_2P_2S_3Se_3$ (f) without SOC and (h) with SOC. (g) Berry curvature of spin up and spin down states along the high-symmetry lines [132].

curvatures for spin up and spin down states also confirm this, as they are equal in magnitude but opposite in sign at the K and K' points (see Fig. 12(g)). When SOC is considered, as shown in Fig. 12(h), the K and K' valley degeneracies are lifted, giving rise to a -16.39 meV valley polarization. This confirms that valley polarization in altermagnets can be effectively tuned by electrostatic potential. In addition, Chen *et al.* also found that electrostatic potential can induce spontaneous valley polarization in the $Mn_2P_2S_3Te_3$ system [236]. Moreover, the valley polarization generated in monolayer altermagnetic $Ca(CoN)_2$ is independent of the SOC effect [237, 238].

4.4. Magnetic field tunable valley polarization

Beyond electric fields, magnetic fields have been repeatedly corroborated as an effective modulating tool. They can directly act on magnetic moments to alter the physical properties of materials. Moreover, they offer high penetrability and a non-contact nature, and the collective responses they evoke are particularly pronounced. Guo *et al.* were the first to propose that valley polarization in altermagnet can be effectively manipulated via the magnetization direction [215]. They pointed out that the CBM and VBM valleys at the X and Y points are protected by the joint symmetry of $\mathcal{C}_{4z}\mathcal{T}$. For an out-of-plane magnetization, the $\mathcal{C}_{4z}\mathcal{T}$ symmetry forbids valley polarization. Conversely, magnetization along the x or y axis breaks the $\mathcal{C}_{4z}\mathcal{T}$ symmetry and induces valley polarization. Importantly, they confirmed this theory in Janus altermagnet $Fe_2MoS_2Se_2$. Subsequently, we also confirmed this theory in the Janus altermagnet $Fe_2WS_2Se_2$, demonstrating that the magnitude and sign of valley polarization can be effectively tuned by the magnetization direction [140].

In 2026, Huang *et al.* systematically investigated the control of valley polarization by in-plane magnetization in the tetragonal altermagnet using a tight-binding model [234]. First, they constructed the Hamiltonian using a collinear AFM order

$$\begin{aligned}\mathcal{H}(\mathbf{k}) = &-4t_1 cos\frac{k_x}{2}cos\frac{k_y}{2}\tau_x - 2t_2(cosk_x + cosk_y)\tau_0 \\ &- 2t_d(cosk_x - cosk_y)\tau_z + \lambda_{SOC}sin\frac{k_x}{2}\frac{k_y}{2}\tau_y\sigma_z \\ &+ J\tau_z N\cdot\sigma + \lambda_{FM}(N_x\sigma_x - N_y\sigma_y).\end{aligned} \tag{7}$$

The Pauli matrices τ and σ act on the sublattice and spin degrees of freedom, respectively. Here $\tau = (\tau_x, \tau_y, \tau_z)$ denote the Pauli matrices for the sublattice pseudospin space, while $\sigma = (\sigma_x, \sigma_y, \sigma_z)$ are the Pauli matrices acting on the real electronic spin degrees of freedom. To quantify the valley polarization, they evaluated the energy eigenvalues of the valleys at the X and Y points. They reduced the 4×4 Hamiltonian to a 2×2 effective Hamiltonian by projecting it onto the sublattice-polarized states

$$\mathcal{H}(X/Y) = -4t_d \mp [(J \mp \lambda_{FM})cos\phi\sigma_x + (J \pm \lambda_{FM})sin\phi\sigma_y]. \tag{8}$$

The VBM energies are obtained by diagonalizing this effective Hamiltonian:

$$E_{X/Y} = -4t_d + \sqrt{(J \mp \lambda_{FM})^2 cos^2\phi + (J \pm \lambda_{FM})^2 sin^2\phi}. \tag{9}$$

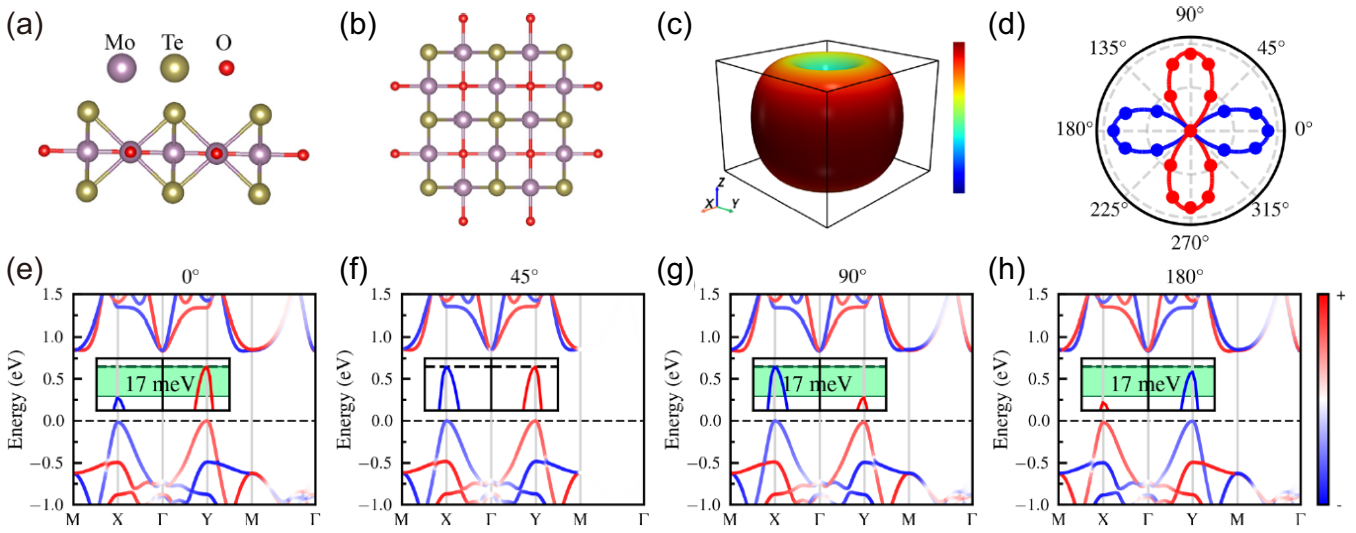


FIG. 13. (a, b) Side and top views of the monolayer Mo_2Te_2O crystal structure. The sliver, brown, and red balls show Mo, Te, and O elements respectively. (c) The MAE landscapes of Mo_2Te_2O. (d) Dependence of valley polarization on the in-plane magnetization angle ϕ. (e-h) Band structures of monolayer Mo_2Te_2O at different in-plane magnetization angles ϕ (with respect to the x axis): (e) $\phi = 0°$, (f) $\phi = 45°$, (g) $\phi = 90°$, and (h) $\phi = 180°$ [234].

In the strong exchange limit ($J \gg \lambda_{FM}$), approximating to first order in Taylor series yields the energies as

$$E_{X/Y} \approx E_0 \mp \lambda_{FM} cos2\phi. \tag{10}$$

Thus, the valley polarization $\Delta E_v = E_X - E_Y$ is given by

$$\Delta E_v \approx -2\lambda_{FM} cos2\phi. \tag{11}$$

From the formula, the valley polarization is maximized when the magnetization angle is 0°, 90°, 180°, and 270°. In contrast, valley polarization becomes zero when the magnetization is along 45°, 135°, 225°, and 315°. This originates from the fact that magnetization along these directions reinstates a mirror symmetry between the two valleys, which protects their degeneracy. Simultaneously, they confirmed this mechanism in the monolayer tetragonal lattice Mo_2Te_2O. As shown in Fig. 13(a, b), it is a trilayer structure composed of a Mo-O layer sandwiched between two Te layers. The angular dependence of the total energy is shown in Fig. 13(c), from which it is found that the out-of-plane direction is the magnetic easy axis. Additionally, the MAE is isotropic in the xy plane. To verify the derivation of the effective Hamiltonian, they calculated the valley polarization of Mo_2Te_2O as a function of the magnetization direction. As shown in Fig. 13(d), the valley splitting shows a $cos2\phi$ dependence, consistent with their TB model derivation. Besides, Fig. 13(e-h) shows the band structures at different magnetization angles. When the magnetization is along the x axis, as shown in Fig. 13(e), the broken $\mathcal{C}_{4z}\mathcal{T}$ symmetry induces a valley polarization of 17 meV. When the magnetization is rotated to 45°, the mirror symmetry is restored, which protects the valley degeneracy at the X and Y points (see Fig. 13(f)). Further rotating the magnetization to the y axis, as shown in Fig. 13(g), the valley polarization undergoes a sign reversal. Finally, rotating the magnetization to the -x axis, both the magnitude and the sign of the valley polarization are changed, while the spin texture is reversed (see Fig. 13(h)). By rotating the magnetization direction, both the presence and the sign of valley polarization can be controlled, which holds promise for valley-switch devices.

4.5. Interlayer stacking tunable valley polarization

The van der Waals interaction in two-dimensional materials strongly influences their chemical and physical properties, and the stacking configuration of layers can give rise to novel phenomenon. The interlayer magnetism of $CrBr_3$ is experimentally observed to be stacking-dependent via interlayer sliding [239]. Moreover, interlayer stacking variations can give rise to magnetic phase transitions [104, 240], topological phase transitions [241], and out-of-plane ferroelectric polarization [242, 243]. Therefore, the stacking-order modulation of valley polarization in altermagnets is also a fascinating subject.

Through symmetry analysis, Tian *et al.* systematically investigated valley polarization in the tetragonal altermagnet bilayer Fe_2MoS_4 system [244]. First, they constructed a bilayer model via $\hat{O} = [E\|\mathcal{M}_z]$, which inherently lacks $[\mathcal{C}_2\|\mathcal{M}_z]$ and $[\mathcal{C}_2\|\mathcal{P}]$ symmetry operations. As shown in Fig. 14(a), the band structure exhibits spin splitting, indicating that it is an altermagnet. They proposed that the $[\mathcal{C}_2\|\mathcal{M}_d]$ symmetry can be broken via in-

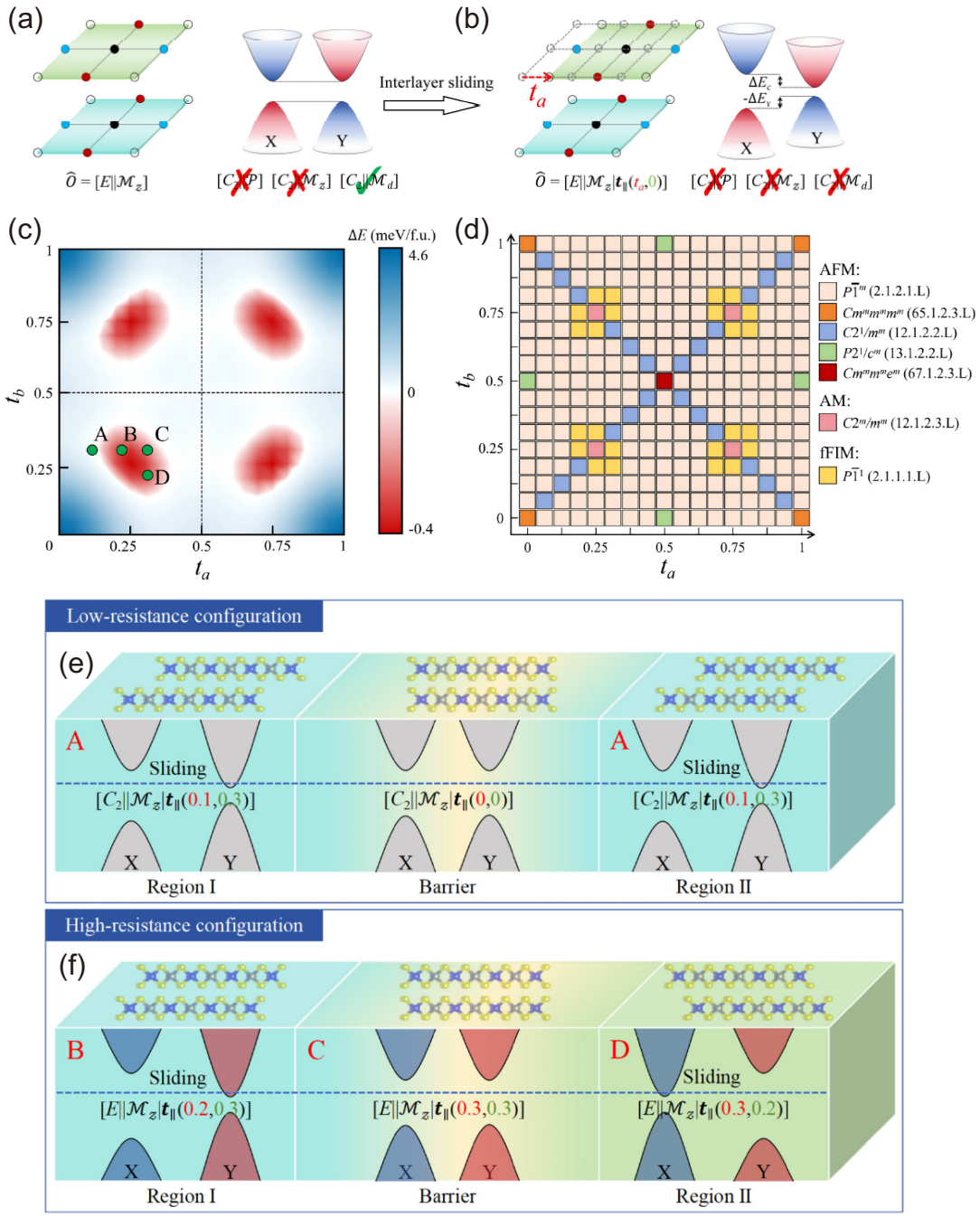


FIG. 14. (a) Bilayer tetragonal altermagnet stacking connected by the $\hat{O} = [\mathrm{E}\|\mathcal{M}_z]$ symmetry operation, and the corresponding band structure schematic. (b) Interlayer sliding and valley polarization schematic. (c) Stacking-dependent interlayer exchange energy. A, B, C, and D represent sliding vectors at $\mathrm{t}_{\|}$ = (0.1, 0.3), (0.2, 0.3), (0.3, 0.3), and (0.3, 0.2), respectively. (d) Spin space group distribution of bilayer stackings Fe_2MoS_4 over the entire space. (e, f) Schematic illustration of a tunneling magnetoresistance device based on bilayer Fe_2MoS_4. (e) Low resistance and (f) high resistance states of tunneling magnetoresistance device [244].

terlayer sliding. Here, the $\mathcal{M}_d$ mirror symmetry is the commonly known $\mathcal{M}_{xy}$ mirror symmetry. The interlayer-sliding bilayer altermagnet shown in Fig. 14(b) is obtained by fixing the bottom layer and translating the top layer by t_a along the a direction. Therefore, the $[\mathcal{C}_2\|\mathcal{M}_d]$ symmetry is broken by interlayer sliding, consequently inducing a valley splitting. They used Fe_2MoS_4 to construct structures that satisfy the symmetry re-

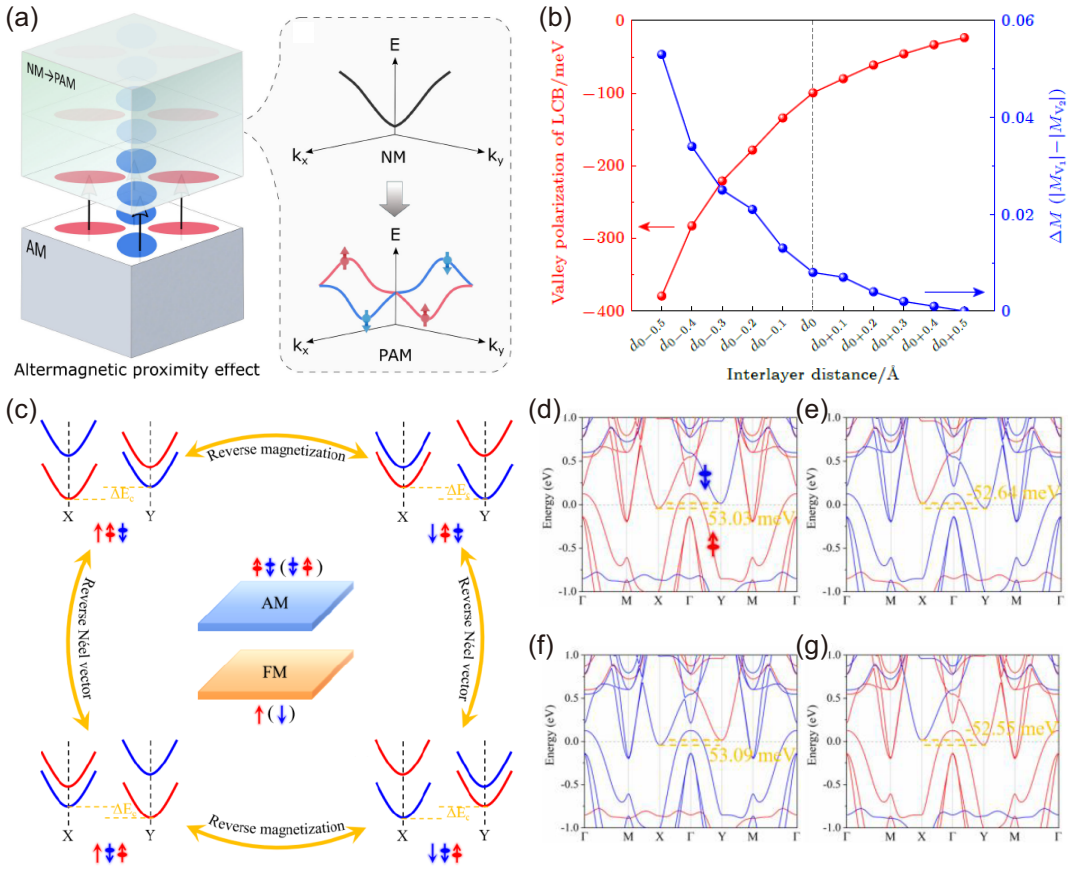


FIG. 15. (a) Schematic of the altermagnetic proximity effect and the corresponding band evolution [251]. (b) Valley polarization as a function of interlayer distance in the V_2Se_2O/SnO heterostructure [252]. (c) The four independent valley polarized states are achieved by switching the magnetizations of the ferromagnetic and Neel orders [252]. (d-g) Band structures of the four independent valley polarized states in the V_2Se_2O/CrP heterostructure [253].

quirements and conducted systematic studies. Two interlayer magnetic configurations are taken into account for each structural stacking registry. As shown in Fig. 14(c), bilayer Fe_2MoS_4 undergoes a transition of interlayer magnetic coupling during sliding. Based on this, the authors further demonstrate that interlayer sliding produces stacking configurations corresponding to distinct AFM, altermagnetic, and fully compensated ferrimagnetic states. Moreover, the spin space groups of all bilayer Fe_2MoS_4 stackings are shown in Fig. 14(d). These distinct spin space groups offer a natural framework to classify the three stacking-dependent magnetic states. Importantly, the modulation of spin and valley through interlayer stacking opens up a new pathway for TMR devices, one that does not rely on an external magnetic field. As shown in Fig. 14(e, f), their proposed tunable TMR response originates from stacking-dependent alignment and misalignment of spin-valley-resolved CBM channels. As shown in Fig. 14(e), the low-resistance state is realized by the alignment of spin channels and CBM valleys between region I and region II. On the contrary, the valley-index mismatch in momentum space gives rise to the high-resistance state. Moreover, $Ca(CoN)_2$ [156], Cr_2WS_4 [245], Fe_2MX_4 (M = Mo, W; X =S, Se, or Te) [246], and Metal-Organic Framework [247] also enable interlayer stacking modulation of valley polarization. It is important to note that Guo *et al.* demonstrated that valley polarization can also be tuned via interlayer twisting in altermagnets [141]. This offers a theoretical prototype for the realization of devices based on valley-polarization control via sliding ferroelectricity.

4.6. Proximity Effect tunable valley polarization

Proximity effects offer a versatile means of engineering material functionalities: a material can acquire magnetic order [248], superconductivity [250], nontrivial topology [251], or enhanced SOC from its neighboring layers [252], thereby extending its physical properties beyond those of the isolated system. Similarly, the altermagnetic proximity effect can induce valley polarization, which is categorized into two cases: altermagnet-nonmagnetic and altermagnet-ferromagnetic heterostructures.

The first category comprises heterostructures composed of altermagnets and nonmagnetic materials. As shown in Fig. 15(a), when a nonmagnetic material is brought into contact with an altermagnet, the electronic wave functions can extend across the interface and transfer the characteristic alternating spin splitting of the altermagnet to the nonmagnetic layer [252]. This interfacial phenomenon induces a phase transition from the nonmagnetic to a proximitized altermagnetic state, wherein the electronic bands, initially degenerate in spin, become spin-polarized in a momentum-dependent manner. It is well known that the proximity effect is short-range and decays with increasing distance from the interface. Xie *et al.* found that the valley polarization of the V_2Se_2O layer is markedly enhanced by decreasing the interlayer distance in the V_2Se_2O/SnO heterostructure, whereas increasing the interlayer distance suppresses it (see Fig. 15(b)) [253]. This further confirms that the altermagnet proximity effect also exhibits a decay behavior as the interface distance increases.

The other category consists of heterostructures made from altermagnets and FM materials. In these heterostructures, the valley polarization direction is strongly dependent on the magnetization directions of both the FM and altermagnet. As shown in Fig. 15(c), when the magnetization of the FM is flipped, the valley polarization at the X and Y points in the altermagnet is reversed [254]. However, a reversal of the Neel vector in the altermagnet flips the local magnetic moments on the magnetic atoms, resulting in two distinct magnetic states. Therefore, when the magnetization reversals of the FM and the Neel order of the altermagnet are combined, four valley polarized states is realized. Based on the above model, as shown in Fig. 15(d-g), they verified that four states can be realized in the V_2S_2O/CrP altermagnet heterostructure. This is attributed to the strong coupling among the CrP magnetization, the V_2S_2O Neel order, and the valley polarization. Moreover, $Ca(CoN)_2$/CoX (X = Cl_2, Se) heterostructure can also effectively tune the spin-valley splitting [255]. Altermagnetic proximity tuning of valley polarization will provide a platform for realizing emergent quantum phenomena in heterostructures [256].

5. CONCLUSIONS AND PERSPECTIVES

In this review, we have introduced the recent advances in altermagnet valleytronics. Firstly, we explored the characteristics of altermagnets and valleytronics. Then, we classify valley polarization into three major categories, namely, type I, type II, and type III induced by the breaking of $\mathcal{T}$ symmetry, $\mathcal{P}$ symmetry, and lattice symmetry, respectively. Finally, we mainly discussed the modulation of altermagnet valley polarization by strain, electric field, electrostatic potential, magnetic field, interlayer stacking, and proximity effect, as well as device applications.

Despite significant progress in both theory and experiment on altermagnets, the number of successfully synthesized materials remains relatively scarce. Among the materials with potential for valley polarization, only V_2Se_2O has been successfully synthesized [257]. However, the preparation of high-quality monolayer and few-layer films remains extremely difficult. This will pose a major obstacle to the development of altermagnet valleytronics.

To advance the development of altermagnet valleytronics, future efforts should focus on the following directions. First, from the perspective of symmetry, the system explores several types of valley polarization that can be achieved in the altermagnets. The symmetry operations that protect valley degeneracy for each type are identified, and the space groups hosting these valley polarizations are determined. Through high-throughput database screening, candidate materials are selected for experimental validation. Then, the coupling mechanisms among ferrovalley, magnetic, ferroelectric, and ferroelastic orders are thoroughly investigated, a Hamiltonian describing the coupling of multiple degrees of freedom is constructed, and the phase diagram for the mutual manipulation of these degrees of freedom is systematically explored. Finally, to realize altermagnet-based valleytronics devices, it is essential to conduct preliminary research on device mechanisms and integration schemes, and to elucidate the pathways for integrating novel valleytronics architectures with CMOS technology. Development should start from valley-based storage or electrically controlled valley switches and progressively extend to complete functional applications.

DECLARATIONS

The authors declare that they have no competing interests and there are no conflicts.

ACKNOWLEDGEMENTS

This work is supported by the National Natural Science Foundation of China (Grants No. 12474238, and No. 12004295). P. Li also acknowledge supports from the Shaanxi Youth Science and Technology New Star Project (Grant No. 2025ZC-KJXX-71), the China's Postdoctoral Science Foundation funded project (Grant No. 2022M722547), the Fundamental Research Funds for the Central Universities (xxj03202205), and the Hefei National Research Center for Physical Sciences at the Microscale (KF2025102). H. Fu and F. Ran thank the National Training Program of Innovation and Entrepreneurship for Undergraduates (Grant No. 202610698288 and No. MSE20250201003).

[1] I. Zutic, J. Fabian, and S. D. Sarma, Spintronics: Fundamentals and applications, *Rev. Mod. Phys.* 76(2), 323 (2004).

[2] T. Dietl, and H. Ohno, Dilute ferromagnetic semiconductors: Physics and spintronic structures, *Rev. Mod. Phys.* 86(1), 187 (2018).

[3] V. Baltz, A. Manchon, M. Tsoi, T. Moriyama, T. Ono, and Y. Tserkovnyak, Antiferromagnetic spintronics, *Rev. Mod. Phys.* 90(1), 015005 (2014).

[4] R. W. McCallum, L. H. Lewis, R. Skomski, M. J. Kramer, and I. E. Anderson, Practical Aspects of Modern and Future Permanent Magnets, *Annu. Rev. Mater. Res.* 44(1), 451 (2014).

[5] C. Moron, C. Cabrera, A. Moron, A. Garcia, and M. Gonzalez, Magnetic Sensors Based on Amorphous Ferromagnetic Materials: A Review, *Sensors* 15(11), 28340 (2015).

[6] M. N. Baibich, J. M. Broto, A. Fert, F. Nguyen Van Dau, F. Petroff, P. Eitenne, G. Creuzet, A. Friederich, and J. Chazelas, Giant Magnetoresistance of (001)Fe/(001)Cr Magnetic Superlattices, *Phys. Rev. Lett.* 61(21), 2472 (1988).

[7] G. Binasch, P. Grunberg, F. Saurenbach, and W. Zinn, Enhanced magnetoresistance in layered magnetic structures with antiferromagnetic interlayer exchange, *Phys. Rev. B* 39(7), 4828 (1989).

[8] C. Chappert, A. Fert, and F. N. Van Dau, The emergence of spin electronics in data storage, *Nat. Mater.* 6(11), 813 (2007).

[9] S. D. Bader, and S. S. P. Parkin, Spintronics, *Annu. Rev. Mater. Res.* 1(1), 71 (2010).

[10] T. Jungwirth, X. Marti, P. Wadley, J. Wunderlich, Antiferromagnetic spintronics, *Nat. Nanotechnol.* 11(3), 231 (2016).

[11] L. Smejkal, Y. Mokrousov, B. Yan, and A. H. MacDonald, Topological antiferromagnetic spintronics, *Nat. Phys.* 14(3), 242 (2018).

[12] P. Nemec, M. Fiebig, T. Kampfrath, and A. V. Kimel, Antiferromagnetic opto-spintronics, *Nat. Phys.* 14(3), 229 (2018).

[13] D. Xiong, Y. Jiang, K. Shi, A. Du, Y. Yao, Z. Guo, D. Zhu, K. Cao, S. Peng, W. Cai, D. Zhu, W. Zhao, Antiferromagnetic spintronics: An overview and outlook, *Fund. Res.* 2(4), 522 (2022).

[14] H. Chen, L. Liu, X. Zhou, Z. Meng, X. Wang, Z. Duan, G. Zhao, H. Yan, P. Qin, and Z. Liu, Emerging Antiferromagnets for Spintronics, *Adv. Mater.* 36(24), 2310379 (2024).

[15] B. H. Rimmler, B. Pal, and S. S. P. Parkin, Non-collinear antiferromagnetic spintronics, *Nat. Rev. Mater.* 10(2), 109 (2025).

[16] J. Zelezny, P. Wadley, K. Olejnik, A. Hoffmann, and H. Ohno, Spin transport and spin torque in antiferromagnetic devices, *Nat. Phys.* 14(3), 220 (2018).

[17] J. Han, R. Cheng, L. Liu, H. Ohno, and S. Fukami, Coherent antiferromagnetic spintronics, *Nat. Mater.* 22(6), (2023).

[18] L. Smejkal, J. Sinova, and T. Jungwirth, Beyond Conventional Ferromagnetism and Antiferromagnetism: A Phase with Nonrelativistic Spin and Crystal Rotation Symmetry, *Phys. Rev. X* 12(3), 031042 (2022).

[19] L. Smejkal, J. Sinova, and T. Jungwirth, Emerging Research Landscape of Altermagnetism, *Phys. Rev. X* 12(4), 040501 (2022).

[20] L. Smejkal, R. Gonzalez-Hernandez, T. Jungwirth, and J. Sinova, Crystal time-reversal symmetry breaking and spontaneous Hall effect in collinear antiferromagnets, *Sci. Adv.* 6(23), eaaz8809 (2020).

[21] L. D. Yuan, Z. Wang, J. W. Luo, E. I. Rashba, and A. Zunger, Giant momentum-dependent spin splitting in centrosymmetric low-Z antiferromagnets, *Phys. Rev. B* 102(1), 014422 (2020).

[22] H. Y. Ma, M. Hu, N. Li, J. Liu, W. Yao, J. F. Jia, and J. Liu, Multifunctional antiferromagnetic materials with giant piezomagnetism and noncollinear spin current, *Nat. Commun.* 12(1), 2846 (2021).

[23] Y. P. Zhu, X. Chen, X. R. Liu, Y. Liu, P. Liu, H. Zha, G. Qu, C. Hong, J. Li, Z. Jiang, X. M. Ma, Y. J. Hao, M. Y. Zhu, W. Liu, M. Zeng, S. Jayaram, M. Lenger, J. Ding, S. Mo, K. Tanaka, M. Arita, Z. Liu, M. Ye, D. Shen, J. Wrachtrup, Y. Huang, R. H. He, S. Qiao, Q. Liu, and C. Liu, Observation of plaid-like spin splitting in a noncoplanar antiferromagnet, Nature 626(7999), 523 (2024).

[24] J. Krempasky, L. Smejkal, S. W. DSouza, M. Hajlaoui, G. Springholz, K. Uhlirova, F. Alarab, P. C. Constantinou, V. Strocov, D. Usanov, W. R. Pudelko, R. G. Hernandez, A. B. Hellenes, Z. Jansa, H. Reichlova, Z. Soban, R. D. G. Betancourt, P. Wadley, J. Sinova, D. Kriegner, J. Minar, J. H. Dil, and T. Jungwirth, Altermagnetic lifting of Kramers spin degeneracy, Nature 626(7999), 517 (2024).

[25] L. Smejkal, A. B. Hellenes, R. Gonzalez-Hernandez, J. Sinova, and T. Jungwirth, Giant and tunneling magnetoresistance in unconventional collinear antiferromagnets with nonrelativistic spin-momentum coupling, *Phys. Rev. X* 12(1), 011028 (2022).

[26] F. Liu, Z. Zhang, X. Yuan, Y. Liu, S. Zhu, Z. Lu, and R. Xiong, Giant tunneling magnetoresistance in insulated altermagnet/ferromagnet junctions induced by spin-dependent tunneling effect, *Phys. Rev. B* 110(13), 134437 (2024).

[27] X. P. Zhang, W. Feng, R. W. Zhang, X. Fan, X. Wang, and Y. Yao, Theory of Anisotropic Magnetoresistance in Altermagnets and Its Applications, *Phys. Rev. Lett.* 135(26), 266706 (2025).

[28] S. Noh, G. H. Kim, J. Lee, H. Jung, U. Seo, G. So, J. Lee, S. Lee, M. Park, S. Yang, Y. S. Oh, H. Jin, C. Sohn, and J. W. Yoo, Tunneling Magnetoresistance in Altermagnetic RuO_2-Based Magnetic Tunnel Junctions, *Phys. Rev. Lett.* 134(24), 246703 (2025).

[29] Y. F. Sun, Y. Mao, Y. C. Zhuang, and Q. F. Sun, Tunneling magnetoresistance effect in altermagnets, *Phys. Rev. B* 112(9), 094411 (2025).

[30] L. Zhang, G. Ni, J. He, and G. Gao, Above room temperature multiferroic tunnel junction with the altermagnetic metal CrSb, *Phys. Rev. B* 112(6), 064401 (2025).

[31] Z. Feng, X. Zhou, L. Smejkal, L. Wu, Z. Zhu, H. Guo, R. G. Hernandez, X. Wang, H. Yan, P. Qin, X. Zhang, H. Wu, H. Chen, Z. Meng, L. Liu, Z. Xia, J. Sinova, T. Jungwirth, and Z. Liu, An anomalous Hall effect in altermagnetic ruthenium dioxide, *Nat. Electron.* 5(11),

735 (2022).
[32] R. D. Gonzalez Betancourt, J. Zubac, R. Gonzalez-Hernandez, K. Geishendorf, Z. Soban, G. Springholz, K. Olejnik, L. Smejkal, J. Sinova, T. Jungwirth, S. T. B. Goennenwein, A. Thomas, H. Reichlova, J. Zelezny, and D. Kriegner, Spontaneous Anomalous Hall Effect Arising from an Unconventional Compensated Magnetic Phase in a Semiconductor, *Phys. Rev. Lett.* 130(3), 036702 (2023).
[33] M. Wang, K. Tanaka, S. Sakai, Z. Wang, K. Deng, Y. Lyu, C. Li, D. Tian, S. Shen, N. Ogawa, N. Kanazawa, P. Yu, R. Arita, and F. Kagawa, Emergent zero-field anomalous Hall effect in a reconstructed rutile antiferromagnetic metal, *Nat. Commun.* 14(1), 8240 (2023).
[34] T. Sato, S. Haddad, I. C. Fulga, F. F. Assaad, and J. van den Brink, Altermagnetic Anomalous Hall Effect Emerging from Electronic Correlations, *Phys. Rev. Lett.* 133(8), 086503 (2024).
[35] H. Reichlova, R. L. Seeger, R. Gonzalez-Hernandez, I. Kounta, R. Schlitz, D. Kriegner, R. Ritzinger, M. Lammel, M. Leiviska, A. B. Hellenes, K. Olejnik, V. Petricek, P. Dolezal, L. Horak, E. Schmoranzerova, A. Badura, S. Bertaina, A. Thomas, V. Baltz, L. Michez, J. Sinova, S. T. B. Goennenwein, T. Jungwirth, and L. Smejkal, Observation of a spontaneous anomalous Hall response in the Mn_5Si_3 d-wave altermagnet candidate, *Nat. Commun.* 15(1), 4961 (2024).
[36] L. Han, X. Fu, R. Peng, X. Cheng, J. Dai, L. Liu, Y. Li, Y. Zhang, W. Zhu, H. Bai, Y. Zhou, S. Liang, C. Chen, Q. Wang, X. Chen, L. Yang, Y. Zhang, C. Song, J. Liu, and F. Pan, Electrical 180° switching of Néel vector in spin-splitting antiferromagnet, *Sci. Adv.* 10(4), eadn0479 (2024).
[37] Y. Fang, J. Cano, and S. A. A. Ghorashi, Quantum Geometry Induced Nonlinear Transport in Altermagnets, *Phys. Rev. Lett.* 133(10), 106701 (2024).
[38] Y. Zhao, Z. Mao, and B. Yan, Nonlinear transport signatures of hidden symmetry breaking in a Weyl altermagnet, *Phys. Rev. B* 112(16), 165127 (2025).
[39] R. Y. Chu, L. Han, Z. H. Gong, X. Z. Fu, H. Bai, S. X. Liang, C. Chen, S. W. Cheong, Y. Y. Zhang, J. W. Liu, Y. Y. Wang, F. Pan, H. Z. Lu, and C. Song, Third-Order Nonlinear Hall Effect in Altermagnet RuO_2, *Phys. Rev. Lett.* 135(21), 216703 (2025).
[40] H. Zhu, J. Li, X. Chen, Y. Yu, and Q. Liu, Magnetic geometry induced quantum geometry and nonlinear transports, *Nat. Commun.* 16(1), 4882 (2025).
[41] L. Han, X. Fu, W. He, J. Dai, Y. X. Zhu, W. Yang, Y. L. Chen, J. C. Zhang, W. Zhu, H. Bai, C. Chen, D. Z. Hou, C. Wan, X. Han, C. Song, J. Liu, and F. Pan, Observation of non-volatile anomalous Nernst effect in altermagnet with collinear Néel vector, *Phys. Rev. Appl.* 23(4), 044066 (2025).
[42] A. Badura, W. H. Campos, V. K. Bharadwaj, I. Kounta, L. Michez, M. Petit, J. Rial, M. Leiviska, V. Baltz, F. Krizek, D. Kriegner, J. Zelezny, J. Zemen, S. Telkamp, S. Sailler, M. Lammel, R. J. Ubiergo, A. B. Hellenes, R. G. Hernandez, J. Sinova, T. Jungwirth, S. T. B. Goennenwein, L. Smejkal, and H. Reichlova, Observation of the anomalous Nernst effect in altermagnetic candidate Mn_5Si_3, *Nat. Commun.* 16(1), 7111 (2025).
[43] S. Iguchi, H. Kobayashi, Y. Ikemoto, T. Furukawa, H. Itoh, S. Iwai, T. Moriwaki, and T. Sasaki, Magneto-optical spectra of an organic antiferromagnet as a candidate for an altermagnet, *Phys. Rev. Research* 7(3), 033026 (2025).
[44] J. Sun, Y. Du, and E. Kan, Symmetry-Breaking Magneto-Optical Effects in Altermagnets, *Nano Lett.* 25(41), 14960 (2025).
[45] M. Liu, J. T. Sun, and S. Meng, Uncompensated Linear Dichroism of Magneto-Optical Kerr Effect in a 2D Altermagnet, *Adv. Funct. Mater.* 36 (29), e21111 (2026)
[46] H. Oan, R. C. Xiao, J. Han, H. Zhu, J. Li, Q. Niu, Y. Gao, and D. Hou, Experimental Evidence of Néel-Order-Driven Magneto-optical Kerr Effect in an Altermagnetic Insulator, *Phys. Rev. Lett.* 136(3), 036701 (2026).
[47] R. G. Hernandez, L. Smejkal, K. Vyborny, Y. Yahagi, J. Sinova, T. Jungwirth, and J. Zelezny, Efficient electrical spin splitter based on nonrelativistic collinear antiferromagnetism, *Phys. Rev. Lett.* 126(12), 127701 (2021).
[48] S. Karube, T. Tanaka, D. Sugawara, N. Kadoguchi, M. Kohda, and J. Nitta, Observation of spin-splitter torque in collinear antiferromagnetic RuO_2, *Phys. Rev. Lett.* 129(13), 137201 (2022).
[49] H. Bai, L. Han, X. Y. Feng, Y. J. Zhou, R. X. Su, Q. Wang, L. Y. Liao, W. X. Zhu, X. Z. Chen, F. Pan, X. L. Fan, and C. Song, Observation of spin splitting torque in a collinear antiferromagnet RuO_2, *Phys. Rev. Lett.* 128(19), 197202 (2022).
[50] S. A. A. Ghorashi, T. L. Hughes, and J. Cano, Altermagnetic routes to majorana modes in zero net magnetization, *Phys. Rev. Lett.* 133(10), 106601 (2024).
[51] H. G. Giil, and J. Linder, Superconductor-altermagnet memory functionality without stray fields, *Phys. Rev. B* 109(13), 134511 (2024).
[52] L. J. Sham, S. J. Allen, J. A. Kamgar, and D. C. Tsui, Valley-Valley Splitting in Inversion Layers on a High-Index Surface of Silicon, *Phys. Rev. Lett.* 40(7), 472 (1978).
[53] H. J. Drouhin, C. Hermann, and G. Lampel, Photoemission from activated gallium arsenide. I. Very-high-resolution energy distribution curves, *Phys. Rev. B* 31(6), 1985 (1985).
[54] X. Q. Zhou, H. M. van Driel, G. Mak, Femtosecond kinetics of photoexcited carriers in germanium, *Phys. Rev. B* 50(8), 5526 (1994).
[55] S. Goswami, K. A. Slinker, M. Friesen, L. M. McGuire, J. L. Truitt, C. Tahan, L. J. Klein, J. O. Chu, P. M. Mooney, D. W. van der Weide, R. Joynt, S. N. Coppersmith, and M. A. Eriksson, Controllable valley splitting in silicon quantum devices, *Nat. Phys.* 3(1), 41 (2007).
[56] J. Isberg, M. Gabrysch, J. Hammersberg, S. Majdi, K. K. Kovi, and D. J. Twitchen, Generation, transport and detection of valley-polarized electrons in diamond, *Nat. Mater.* 12(8), 760 (2013).
[57] M. Jaros, Electronic properties of semiconductors alloy systems, *Rep. Prog. Phys.* 48(8), 1091 (1985).
[58] W. Yao, D. Xiao, and Q. Niu, Valley-dependent optoelectronics from inversion symmetry breaking, *Phys. Rev. B* 77(23), 235406 (2008).
[59] P. Li, B. Liu, S. Chen, W. X. Zhang, and Z. X. Guo, Progress on two-dimensional ferrovalley materials, *Chin. Phys. B* 33(1), 017505 (2024).
[60] K. S. Novoselov, A. K. Geim, S. V. Morozov, D. Jiang, Y. Zhang, S. V. Dubonos, I. V. Grigorieva, and A. A. Firsov, Electric Field Effect in Atomically Thin Carbon Films, *Science* 306(5696), 666 (2004).

[61] D. Gunlycke, C. T. White, Graphene valley filter using a line defect, *Phys. Rev. Lett.* 106(13), 136806 (2011).

[62] Z. Wu, F. Zhai, F. M. Peeters, H. Q. Xu, and K. Chang, Valley-Dependent Brewster Angles and Goos-Hanchen Effect in Strained Graphene, *Phys. Rev. Lett.* 106(17), 176802 (2011).

[63] M. Ezawa, Valley-Polarized Metals and Quantum Anomalous Hall Effect in Silicene, *Phys. Rev. Lett.* 109(5), 055502 (2012).

[64] Y. Jiang, T. Low, K. Chang, M. I. Katsnelson, and F. Guinea, Generation of Pure Bulk Valley Current in Graphene, *Phys. Rev. Lett.* 110(4), 046601 (2013).

[65] H. Pan, Z. Li, C. C. Liu, G. Zhu, Z. Qiao, and Y. Yao, Valley-Polarized Quantum Anomalous Hall Effect in Silicene, *Phys. Rev. Lett.* 112(10), 106802 (2014).

[66] T. Cao, G. Wang, W. Han, H. Ye, C. Zhu, J. Shi, Q. Niu, P. Tan, E. Wang, B. Liu, and J. Feng, Valley-selective circular dichroism of monolayer molybdenum disulphide, *Nat. Commun.* 3(1), 887 (2012).

[67] D. Xiao, G. B. Liu, W. Feng, X. Xu, and W. Yao, Coupled Spin and Valley Physics in Monolayers of MoS_2 and Other Group-VI Dichalcogenides, *Phys. Rev. Lett.* 108(19), 196802 (2012).

[68] K. F. Mak, K. He, J. Shan, and T. F. Heinz, Control of valley polarization in monolayer MoS_2 by optical helicity, *Nat. Nanotechnol.* 7(8), 494(2012).

[69] H. Zeng, J. Dai, W. Yao, D. Xiao, and X. Cui, Valley polarization in MoS_2 monolayers by optical pumping, *Nat. Nanotechnol.* 7(8), 490 (2012).

[70] J. Zhou, Q. Sun, and P. Jena, Valley-Polarized Quantum Anomalous Hall Effect in Ferrimagnetic Honeycomb Lattices, *Phys. Rev. Lett.* 119(4), 046403 (2017).

[71] K. L. Seyler, D. Zhong, B. Huang, X. Linpeng, N. P. Wilson, T. Taniguchi, K, Watanabe, W. Yao, D. Xiao, M. A. McGuire, K. C. Fu, and X. Xu, Valley Manipulation by Optically Tuning the Magnetic Proximity Effect in WSe_2/CrI_3 Heterostructures, *Nano Lett.* 18(6), 3823 (2018).

[72] B. Zhai, J. Du, C. Shen, T. Wang, Y. Peng, Q. Zhang, and C. Xia, Spin-dependent Dirac electrons and valley polarization in the ferromagnetic stanene/CrI_3 van der Waals heterostructure, *Phys. Rev. B* 100(19), 195307 (2019).

[73] T. Norden, C. Zhao, P. Zhang, R. Sabirianov, A. Petrou, and H. Zeng, Giant valley splitting in monolayer WS_2 by magnetic proximity effect, *Nat. Commun.* 10(1), 4163 (2019).

[74] M. Vila, J. H. Garcia, and S. Roche, Valley-polarized quantum anomalous Hall phase in bilayer graphene with layer-dependent proximity effects, *Phys. Rev. B* 104(16), L16113 (2021).

[75] Y. C. Cheng, Q. Y. Zhang, and U. Schwingenschlogl, Valley polarization in magnetically doped single-layer transition-metal dichalcogenides, *Phys. Rev. B* 89(15), 155429 (2014).

[76] S. Sattar, N. Singh, and U. Schwingenschlogl, Proximity-induced spin-valley polarization in silicene or germanene on F-doped WS_2, *Phys. Rev. B* 94(20), 205415 (2016).

[77] X. Chen, L. Zhong, X. Li, and J. Qi, Valley splitting in the transition-metal dichalcogenide monolayer via atom adsorption, *Nanoscale* 9(6), 2188 (2017).

[78] R. Peng, Y. Ma, S. Zhang, B. Huang, and Y. Dai, Valley Polarization in Janus Single-Layer MoSSe via Magnetic Doping, *J. Phys. Chem. Lett.* 9(13), 3612 (2018).

[79] H. Rostami, and R. Asgari, Valley Zeeman effect and spin-valley polarized conductance in monolayer MoS_2 in a perpendicular magnetic field, *Phys. Rev. B* 91(7), 075433 (2015).

[80] G. Aivazian, Z. Gong, A. M. Jones, R. L. Chu, J. Yan, D. G. Mandrus, C. Zhang, D. Cobden, W. Yao, and X. Xu, Magnetic control of valley pseudospin in monolayer WSe_2, *Nat. Phys.* 11(2), 148 (2015).

[81] A. Srivastava, M. Sidler, A. V. Allain, D. S. Lembke, A. Kis, and A. Imamoglu, Valley Zeeman effect in elementary optical excitations of monolayer WSe_2, *Nat. Phys.* 11(2), 141 (2015).

[82] A. Arora, R. Schmidt, R. Schneider, M. R. Molas, I. Breslavetz, M. Potemski, and R. Bratschitsch, Valley Zeeman Splitting and Valley Polarization of Neutral and Charged Excitons in Monolayer $MoTe_2$ at High Magnetic Fields, *Nano Lett.* 16(6), 3624 (2016).

[83] T. Smolenski, M. Goryca, M. Koperski, C. Faugeras, T. Kazimierczuk, A. Bogucki, K. Nogajewski, P. Kossacki, and M. Potemski, Tuning Valley Polarization in a WSe_2 Monolayer with a Tiny Magnetic Field, *Phys. Rev. X* 6(2), 021024 (2016).

[84] O. L. Sanchez, D. Ovchinnikov, S. Misra, A. Allain, and A. Kis, Valley Polarization by Spin Injection in a Light-Emitting van der Waals Heterojunction, *Nano Lett.* 16(9), 5792 (2016).

[85] A. Friedlan, and M. M. Dignam, Valley polarization in biased bilayer graphene using circularly polarized light, *Phys. Rev. B* 103(7), 075414 (2021).

[86] W. Y. Tong, S. J. Gong, X. Wan, and C. G. Duan, Concepts of ferrovalley material and anomalous valley Hall effect, *Nat. Commun.* 7(1), 13612 (2016).

[87] P. Zhao, Y. Ma, C. Lei, H. Wang, B. Huang, and Y. Dai, Single-layer $LaBr_2$: Two-dimensional valleytronic semiconductor with spontaneous spin and valley polarizations, *Appl. Phys. Lett.* 115(26), 261605 (2019).

[88] P. Jiang, L. Kang, Y. L. Li, X. Zheng, Z. Zeng, and S. Sanvito, Prediction of the two-dimensional Janus ferrovalley material LaBrI, *Phys. Rev. B* 104(3), 035430 (2021).

[89] A. Sharan, S. Lany, and N. Singh, Computational discovery of two-dimensional rare-earth iodides: promising ferrovalley materials for valleytronics, *2D Mater.* 10(1), 015021 (2022).

[90] H. Hu, W. Y. Tong, Y. H. Shen, X. Wan, and C. G. Duan, Concepts of the half-valley-metal and quantum anomalous valley Hall effect, *npj Comput. Mater.* 6(1), 129 (2020).

[91] W. Pan, Tuning the magnetic anisotropy and topological phase with electronic correlation in single-layer H-$FeBr_2$, *Phys. Rev. B* 106(12), 125122 (2022).

[92] J. Luo, H. Meng, X. X. Xue, K. Q. Chen, and L. M. Tang, Intrinsic ferrovalley non-Janus FeXI (X = Cl, Br) with large valley polarization and nonvolatile reversible control of the anomalous valley Hall effect in multiferroic heterojunctions, *Phys. Rev. B* 110(8), 085401 (2024).

[93] Q. Cui, Y. Zhu, J. Liang, P. Cui, and H. Yang, Spin-valley coupling in a two-dimensional VSi_2N_4 monolayer, *Phys. Rev. B* 103(8,) 085421 (2021).

[94] X. Feng, X. Xu, Z. He, R. Peng, Y. Dai, B. Huang, and Y. Ma, Valley-related multiple Hall effect in monolayer VSi_2P_4 *Phys. Rev. B* 104(7), 075421 (2021).

[95] S. Li, Q. Wang, C. Zhang, P. Guo, and S. A. Yang, Correlation-driven topological and valley states in monolayer VSi_2P_4 *Phys. Rev. B* 104(8), 085149 (2021).

[96] X. Zhou, R. W. Zhang, Z. Zhang, W. Feng, Y. Mokrousov, and Y. Yao, Sign-reversible valley-dependent Berry phase effects in 2D valley-half-semiconductors, *npj Comput. Mater.* 7(1), 160 (2021).

[97] P. Li, X. Yang, Q. S. Jiang, Y. Z. Wu, and W. Xun, Built-in electric field and strain tunable valley-related multiple topological phase transitions in $VSiXN_4$(X = C, Si, Ge, Sn, Pb) monolayers, *Phys. Rev. Mater.* 7(6), 064002 (2023).

[98] S. D. Guo, Y. L. Tao, H. T. Guo, Z. Y. Zhao, B. Wang, G. Wang, and X. Wang, Possible electronic state quasi-half-valley metal in a VGe_2P_4 monolayer, *Phys. Rev. B* 107(6), 054414 (2023).

[99] B. Huang, W. Y. Liu, X. C. Wu, S. Z. Li, H. Li, Z. Yang, and W. B. Zhang, Large spontaneous valley polarization and high magnetic transition temperature in stable two-dimensional ferrovalley YX_2(Y = I, Br, and Cl), *Phys. Rev. B* 107(4), 045423 (2023).

[100] Y. Wu, J. Tong, L. Deng, F. Luo, F. Tian, G. Qin, and X. Zhang, Coexisting Ferroelectric and Ferrovalley Polarizations in Bilayer Stacked Magnetic Semiconductors, *Nano Lett.* 23(13), 6226 (2023).

[101] H. Cheng, L. Zhang, X. Yuan, G. Hu, J. Ren, and X. Zhao, Across-layer sliding ferroelectricity and robust valley polarization in inversion-symmetry lattices, *Phys. Rev. B* 112(19), 195401 (2025).

[102] H. X. Cheng, J. Zhou, W. Ji, Y. N. Zhang, and Y. P. Feng, Two-dimensional intrinsic ferrovalley GdI_2 with large valley polarization, *Phys. Rev. B* 103(12), 125121 (2021).

[103] S. D. Guo, J. X. Zhu, W. Q. Mu, and B. G. Liu, Possible way to achieve anomalous valley Hall effect by piezoelectric effect in a $GdCl_2$ monolayer, *Phys. Rev. B* 104(22), 224428(2021).

[104] W. Xun, C. Wu, H. Sun, W. Zhang, Y. Z. Wu, and P. Li, Coexisting Magnetism, Ferroelectric, and Ferrovalley Multiferroic in Stacking-Dependent Two-Dimensional Materials, *Nano Lett.* 24(11), 3541 (2024).

[105] R. Peng, Y. Ma, X. Xu, Z. He, B. Huang, and Y. Dai, Intrinsic anomalous valley Hall effect in single-layer Nb_3I_8, *Phys. Rev. B* 102(3), 035412 (2020).

[106] Y. Wang, H. Sun, C. Wu, W. Zhang, S. D. Guo, Y. She, and P. Li, Multifield tunable valley splitting and anomalous valley Hall effect in two-dimensional antiferromagnetic MnBr, *Phys. Rev. B* 111(8), 085432 (2025).

[107] W. Du, R. Peng, Z. He, Y. Dai, B. Huang, and Y. Ma, Anomalous valley Hall effect in antiferromagnetic monolayers, *npj 2D Mater. Appl.* 11(1), 6 (2022).

[108] W. Zhou, G. Zheng, A. Li, D. Zheng, and F. Ouyang, Orbital contribution to the regulation of the spin-valley coupling in antiferromagnetic monolayer $MnPTe_3$, *Phys. Rev. B* 107(3), 035139 (2023).

[109] W. X. Jiang, Z. H. Gong, Y. Chen, Z. Gui, and L. Huang, Sliding engineering spin-valley-layer coupling and altermagnetism in bilayer antiferromagnetic honeycomb lattices, *Phys. Rev. B* 113(5), 054441 (2026).

[110] K. Wang, Y. Li, H. Mei, P. Li, and Z. X. Guo, Quantum anomalous Hall and valley quantum anomalous Hall effects in two-dimensional d^0 orbital XY monolayers, *Phys. Rev. Mater.* 6(4), 044202 (2022).

[111] K. Sheng, Q. Chen, H. K. Yuan, and Z. Y. Wang, Monolayer CeI_2: An intrinsic room-temperature ferrovalley semiconductor, *Phys. Rev. B* 105(7), 075304 (2022).

[112] P. Li, C. Wu, C. Peng, M. Yang, and W. Xun, Multifield tunable valley splitting in two-dimensional MXene Cr_2COOH, *Phys. Rev. B* 108(19), 195424 (2023).

[113] H. Huan, Y. Xue, B. Zhao, G. Gao, H. Bao, and Z. Yang, Strain-induced half-valley metals and topological phase transitions in MBr_2 monolayers (M =Ru, Os), *Phys. Rev. B* 104(16), 165427 (2021).

[114] W. Xie, L. Zhang, Y. Yue, M. Li, and H. Wang, Giant valley polarization and perpendicular magnetocrystalline anisotropy energy in monolayer MX_2 (M = Ru, Os; X = Cl, Br), *Phys. Rev. B* 109(2), 024406 (2024).

[115] C. Wu, H. Sun, P. Dong, Y. Z. Wu, and P. Li, Coexisting Triferroic and Multiple Types of Valley Polarization by Structural Phase Transition in 2D Materials, *Adv. Funct. Mater.* 35(31), 2501506 (2025).

[116] Y. A. Bychkov, and E. I. Rashba, Properties of a 2D electron gas with lifted spectral degeneracy, *JETP Lett.* 39(2), 78 (1984).

[117] G. Dresselhaus, Spin-orbit coupling effects in zinc blende structures, *Phys. Rev.* 100(2), 580 (1955).

[118] H. Yuan, M. S. Bahramy, K. Morimoto, S. Wu, K. Nomura, B. J. Yang, H. Shimotani, R. Suzuki, M. Toh, C. Kloc, X. Xu, R. Arita, N. Nagaosa, and Y. Iwasa, Zeeman-type spin splitting controlled by an electric field, *Nat. Phys.* 9(9), 563 (2013).

[119] D. Litvin, and W. Opechowski, Spin Groups, *Physica* 76(3), 538 (1974).

[120] D. B. Litivin, Spin Point Groups, *Act Crystallogr. Sect. A* 33(3), 279 (1977).

[121] A. F. Andreev, and V. Marchenko, Symmetry and the Macroscopic Dynamics of Magnetic Materials, *Sov. Phys. Usp.* 23(1), 21 (1980).

[122] A. B. Hellenes, T. Jungwirth, R. Jaeschke-Ubiergo, A. Chakraborty, J. Sinova, L. Smejkal, P-wave magnets, arXiv:2309.01607.

[123] J. C. Slater, Ferromagnetism and the band theory, *Rev. Mod. Phys.* 25(1), 199 (1953).

[124] T. Dietl, and H. Ohno, Dilute ferromagnetic semiconductors: Physics and spintronic structures, *Rev. Mod. Phys.* 86(1), 187 (2014).

[125] R. Ramazashvili, Kramers degeneracy in a magnetic field and zeeman spin-orbit coupling in antiferromagnetic conductors, *Phys. Rev. B* 79(18), 184432 (2009).

[126] L. D. Yuan, X. Zhang, C. M. Acosta, and A. Zunger, Uncovering spin-orbit coupling-independent hidden spin polarization of energy bands in antiferromagnets, *Nat. Commun.* 14(1), 5301 (2023).

[127] L. Bai, W. Feng, S. Liu, L. Smejkal, Y. Mokrousov, and Y. Yao, Altermagnetism: Exploring new frontiers in magnetism and spintronics, *Adv. Funct. Mater.* 34(49), 2409327 (2024).

[128] S. Zeng, and Y. J. Zhao, Description of two-dimensional altermagnetism: Categorization using spin group theory, *Phys. Rev. B* 110(5), 054406 (2024).

[129] J. Sodequist, and T. Olsen, Two-dimensional altermagnets from high throughput computational screening: Symmetry requirements, chiral magnons, and spin-orbit effects, *Appl. Phys. Lett.* 124(18), 182409 (2024).

[130] Y. Zhu, M. Gu, Y. Liu, X. Chen, Y. Li, S. Du, and Q. Liu, Sliding Ferroelectric Control of Unconventional Magnetism in Stacked Bilayers, *Phys. Rev. Lett.* 135(5),

056801 (2025).
[131] J. W. Gonzalez, T. Brumme, E. S. Morell, and A. M. Leon, Engineering altermagnetism via layer shifts and spin order in bilayer $MnPS_3$, *npj 2D Mater. Appl.* 10(1), 11 (2026).
[132] H. Sun, P. Dong, C. Wu, and P. Li, Multifield-induced antiferromagnet transformation into altermagnet and realized anomalous valley Hall effect in monolayer $VPSe_3$, *Phys. Rev. B* 111(23), 235431 (2025).
[133] S. Sheoran, and P. Dev, Spontaneous anomalous Hall effect in two-dimensional altermagnets, *Phys. Rev. B* 111(18), 184407 (2025).
[134] H. Z. Liu, R. He, J. Y. Zhan, D. Wang, M. D. He, N. Luo, J. Zeng, K. Q. Chen, and L. M. Tang, Anomalous Hall effect in A-type antiferromagnetic bilayers, *Phys. Rev. B* 112(13), 134411 (2025).
[135] R. A. Duine, K. J. Lee, S. S. P. Parkin, and M. D. Stiles, Synthetic antiferromagnetic spintronics, *Nat. Phys.* 14(7), 217 (2018).
[136] P. K. Amiri, C. Phatak, and G. Finocchio, Prospects for Antiferromagnetic Spintronic Devices, *Annu. Rev. Mater. Res.* 54(1), 117 (2024).
[137] H. Chen, L. Liu, X. Zhou, Z. Meng, X. Wang, Z. Duan, G. Zhao, H. Yan, P. Qin, Z. Liu, Emerging Antiferromagnets for Spintronics, *Adv. Mater.* 36(14), 2310379 (2024).
[138] Y. Zhu, T. Chen, Y. Li, L. Qiao, X. Ma, C. Liu, T. Hu, H. Gao, and W. Ren, Multipiezo Effect in Altermagnetic V_2SeTeO Monolayer, *Nano Lett.* 24(1), 472 (2024).
[139] W. Xun, X. Liu, Y. Zhang, Y. Z. Wu, and P. Li, Stacking-, strain-engineering induced altermagnetism, multipiezo effect, and topological state in two-dimensional materials, *Appl. Phys. Lett.* 126(16), 161903 (2025).
[140] Y. She, Y. Wang, H. Sun, C. Wu, W. Zhang, and P. Li, Type III valley polarization and anomalous valley Hall effect in the two-dimensional non-Janus and Janus altermagnet $Fe_2WS_2Se_2$, *Phys. Rev. B* 113(3), 035420 (2026).
[141] S. D. Guo, Y. Liu, J. Yu, and C. C. Liu, Valley polarization in twisted altermagnetism, *Phys. Rev. B* 110(22), L220402 (2024).
[142] R. W. Zhang, C. Cui, R. Li, J. Duan, L. Li, Z. M. Yu, and Y. Yao, Predictable Gate-Field Control of Spin in Altermagnets with Spin-Layer Coupling, *Phys. Rev. Lett.* 133(5), 056401 (2024).
[143] H. Zeng, W. Zhang, C. Qiu, D. Z. Ding, and J. Zhao, Symmetry breaking induced nonrelativistic spin splitting and spontaneous valley polarization in altermagnetic $Ca(CoN)_2$ bilayer, *Appl. Phys. Lett.* 126(20), 202405 (2025).
[144] X. Hu, W. Zhao, W. Xia, H. Sun, C. Wu, Y. Z. Wu, and P. Li, Valley Polarization and Anomalous Valley Hall Effect in Altermagnet Ti_2Se_2S with Multipiezo Properties, *Appl. Phys. Lett.* 127(1), 011905 (2025).
[145] W. Xia, W. Zhao, X. Hu, H, Sun, C. Wu, G. Guo, and P. Li, Strain and ferroelectric polarization tune magnetic phase transition and anomalous Hall effect in Ti_2Se_2S/PbTe heterostructure with Rashba effect, *Appl. Phys. Lett.* 128(16), 161903 (2026).
[146] S. D. Guo, X. S. Guo, K. Cheng, K. Wang, and Y. S. Ang, Piezoelectric altermagnetism and spin-valley polarization in Janus monolayer Cr_2SO, *Appl. Phys. Lett.* 123(8), 082401 (2023).
[147] S. D. Guo, Valley polarization in two-dimensional zero-netmagnetization magnets, *Appl. Phys. Lett.* 126(8), 080502 (2025).
[148] P. Dong, H. Sun, C. Wu, and P. Li, Sliding Ferroelectricity Induced and Switched Altermagnetism in GaSe-$VPSe_3$-GaSe Sandwiched Heterostructure with Strong Magnetoelectric Effect, *Acta Mater.* 309(1), 122064 (2026).
[149] W. X. Jiang, Z. H. Gong, Y. Chen, Z. Gui, and L. Huang, Sliding engineering spin-valley-layer coupling and altermagnetism in bilayer antiferromagnetic honeycomb lattices, *Phys. Rev. B* 113(5), 054441 (2026).
[150] Y. Wu, L. Deng, X. Yin, J. Tong, F. Tian, and X. Zhang, Valley-Related Multipiezo Effect and Noncollinear Spin Current in an Altermagnet Fe_2Se_2O Monolayer, *Nano Lett.* 24(34), 10534 (2024).
[151] F. Zhang, X. Cheng, Z. Yin, C. Liu, L. Deng, Y. Qiao, Z. Shi, S. Zhang, J. Lin, Z. Liu, M. Ye, Y. Huang, X. Meng, C. Zhang, T. Okuda, K. Shimada, S. Cui, Y. Zhao, G. H. Cao, S. Qiao, J. Liu, and C. Chen, Crystal-symmetry-paired spin-valley locking in a layered room-temperature metallic altermagnet candidate, *Nat. Phys.* 21(5), 760 (2025).
[152] A. D. Fan, Y. K. Wang, J. Y. Li, and S. Li, Valley-dependent electronic properties in two-dimensional altermagnetic iron-based transition metal chalcogenides, *Phys. Rev. B* 112(23), 235135 (2025).
[153] X. W. Shen, W. Y. Tong, S. J. Gong, and C. G. Duan, Electrically tunable polarizer based on 2D orthorhombic ferrovalley materials, *2D Mater.* 5(1), 011001 (2018).
[154] Y. Jia, F. Luo, X. Hao, Q. Meng, W. Dou, L. Zhang, J. Wu, S. Zhai, and M. Zhou, Intrinsic Valley Polarization and High-Temperature Ferroelectricity in Two-Dimensional Orthorhombic Lead Oxide, *ACS Appl. Mater. Interfaces* 13(5), 6480 (2021).
[155] G. Yu, J. Ji, C. Xu, and H. J. Xiang, Bilayer stacking ferrovalley materials without breaking time-reversal and spatial-inversion symmetry, *Phys. Rev. B* 109(7), 075434 (2024).
[156] N. Cheng, Y. Yin, X. Zhao, G. Hu, X. Yuan, and J. Ren, Sliding-controlled spin-valley-layer polarized anomalous Hall effect in two-dimensional altermagnetic bilayers, *Phys. Rev. B* 113(15), 155424 (2026).
[157] Y. Wu, J. Tong, L. Deng, F. Luo, F. Tian, G. Qin, and X. Zhang, Realizing spontaneous valley polarization and topological phase transitions in monolayer ScX_2(X = Cl, Br, I), *Acta Mater.* 246(1), 118731 (2023).
[158] Y. Huangfu, P. Liu, D. Li, C. Liu, H. Lu, and G. Zhang, Tunable valley states in two-dimensional $ScBr_2$, *Appl. Phys. Lett.* 125(14), 143101 (2024).
[159] Z. He, R. Peng, Y. Dai, B. Huang, and Y. Ma, Single-layer ScI_2: A paradigm for valley-related multiple Hall effect, *Appl. Phys. Lett.* 119(24), 243102 (2021).
[160] K. Sheng, B. Zhang, and Z. Y. Wang, Valley polarization in a two-dimensional high-temperature semiconducting $TiInTe_3$ honeycomb ferromagnet, *Acta Mater.* 262(1), 119461 (2024).
[161] S. Li, Y. Huangfu, K. Ren, C. Liu, B. Wang, and X. Zhou, Valley manipulation in 2D multiferroic $TiInSe_3$: Doping-induced valley polarization and stacking-engineered effects, *Appl. Phys. Lett.* 127(24), 242404 (2025).
[162] S. Ji, R. Yao, C. Quan, J. Yang, F. Caruso, and X. Li, Anomalous valley Hall effect induced by mirror symme-

try breaking in transition metal dichalcogenides, *Phys. Rev. B* 107(17), 174434 (2023).

[163] W. Du, Y. Ma, R. Peng, H. Wang, B. Huang, and Y. Dai, Prediction of single-layer $TiVI_6$ as a promising two-dimensional valleytronic semiconductor with spontaneous valley polarization, *J. Mater. Chem. C* 18(38), 13220 (2020).

[164] C. Shen, G. Wang, T. Wang, C. Xia, and J. Li, Spin orientation and strain tuning valley polarization with magneto-optic Kerr effects in ferrovalley VS_2 monolayer, *Appl. Phys. Lett.* 117(4), 042406 (2020).

[165] C. Wang, and Y. An, Effects of strain and stacking patterns on the electronic structure, valley polarization and magnetocrystalline anisotropy of layered VTe_2, *Appl. Surf. Sci.* 538(4), 148098 (2021).

[166] X. Shen, X. Lu, F. Huang, and J. Zhang, Coexistence and coupling of multiple ferroic orders in van der Waals monolayers, *Phys. Rev. B* 110(4), 045435 (2024).

[167] C. Zhang, Y. Nie, S. Sanvito, and A. Du, First-Principles Prediction of a Room-Temperature Ferromagnetic Janus VSSe Monolayer with Piezoelectricity, Ferroelasticity, and Large Valley Polarization, *Nano Lett.* 19(2), 1366 (2019).

[168] C. Luo, X. Peng, J. Qu, and J. Zhong, Valley degree of freedom in ferromagnetic Janus monolayer H-VSSe and the asymmetry-based tuning of the valleytronic properties, *Phys. Rev. B* 101(24), 245416 (2020).

[169] C. Li, and Y. An, Two-dimensional intrinsic ferrovalley Janus 2H-VSeS monolayer with high Curie temperature and robust valley polarization, *Phys. Rev. Mater.* 6(16), 094012 (2022).

[170] Y. F. Zhao, Y. H. Shen, H. Hu, W. Y. Tong, and C. G. Duan, Combined piezoelectricity and ferrovalley properties in Janus monolayer VClBr, *Phys. Rev. B* 103(11), 115124 (2021).

[171] Q. Cui, Y. Zhu, J. Liang, P. Cui, and H. Yang, Spin-valley coupling in a two-dimensional VSi_2N_4 monolayer, *Phys. Rev. B* 103(8), 085421 (2021).

[172] X. Zhou, R. W. Zhang, Z. Zhang, W. Feng, Y. Mokrousov, and Y. Yao, Sign-reversible valley-dependent Berry phase effects in 2D valley-half-semiconductors, *npj Comput. Mater.* 7(1), 160 (2017).

[173] X. Feng, X. Xu, Z. He, R. Peng, Y. Dai, B. Huang, and Y. Ma, Valley-related multiple Hall effect in monolayer VSi_2P_4, *Phys. Rev. B* 104(7), 075421 (2021).

[174] S. Li, Q. Wang, C. Zhang, P. Guo, and S. A. Yang, Correlation-driven topological and valley states in monolayer VSi_2P_4, *Phys. Rev. B* 104(8), 085149 (2021).

[175] S. D. Guo, W. Q. Mu, J. H. Wang, Y. X. Yang, B. Wang, and Y. S. Ang, Strain effects on the topological and valley properties of the Janus monolayer $VSiGeN_4$, *Phys. Rev. B* 106(6), 064416 (2022).

[176] Z. He, R. Peng, X. Feng, X. Xu, Y. Dai, B. Huang, and Y. Ma, Two-dimensional valleytronic semiconductor with spontaneous spin and valley polarization in single-layer Cr_2Se_3, *Phys. Rev. B* 104(7), 075105 (2021).

[177] C. Liu, G. D. Zhao, S. Picozzi, X. Li, and J. Yang, Spin-canting-driven triple coupling of spin, electric, and valley polarization in two-dimensional antiferromagnetic semiconductors, *Phys. Rev. B* 110(9), 094409 (2024).

[178] Y. Xu, H. Liu, Y. Dai, B. Huang, and W. Wei, Spin-valley splitting and spontaneous valley polarization in antiferromagnetic $Mn_2P_2X_3Y_3$ monolayers, *Appl. Phys. Lett.* 122(24), 242404 (2023).

[179] H. Sun, Y. Ren, C. Wu, P. Dong, W. Zhang, Y. Z. Wu, and P. Li, Ferroelectric tuning of the valley polarized metal-semiconductor transition in $Mn_2P_2S_3Se_3/Sc_2CO_2$ van der Waals heterostructures and application to nonlinear Hall effect devices, *Phys. Rev. Appl.* 23(3), 034032 (2025).

[180] X. Peng, B. Xia, M. Si, and D. Gao, Electronic correlation-driven quantum anomalous valley Hall effect in intrinsic ferrovalley FeClBr, *Appl. Phys. Lett.* 124(22), 223101 (2024).

[181] Y. Xu, S. Wang, S. Yu, X. Wang, B. Huang, Y. Dai, and W. Wei, Spontaneous Valley Polarization in a Ferromagnetic $Fe(OH)_2$ Monolayer, *J. Phys. Chem. Lett.* 13(49), 11543 (2022).

[182] S. D. Guo, L. Zhang, Y. Zhang, P. Li, and G. Wang, Large spontaneous valley polarization and anomalous valley Hall effect in antiferromagnetic monolayer Fe_2CF_2, *Phys. Rev. B* 110(2), 024416 (2024).

[183] S. D. Guo, M. X. Wang, Y. L. Tao, and B. G. Liu, Piezoelectric ferromagnetism in Janus monolayer YBrI: a first-principles prediction, *Phys. Chem. Chem. Phys.* 25(1), 796 (2023).

[184] J. Li, Y. Q. Chen, H. K. Yuan, and C. L. Tian, Prediction of the two-dimensional ferromagnetic semiconductor Janus 2H-ZrTeI monolayer with large valley and piezoelectric polarizations, *Nanoscale* 16(39), 18504 (2024).

[185] Y. Zhang, Y. Ma, R. Peng, H. Wang, B. Huang, and Y. Dai, Large valley-polarized state in single-layer NbX_2(X = S, Se): Theoretical prediction, *Nano. Res.* 14(3), 834 (2021).

[186] B. Huang, S. Z. Li, Z. Yang, Z. Li, H. Li, and W. B. Zhang, Giant Spontaneous Valley Polarization and Adsorption-Induced Topological Phase Transition in Single-Layer 2H-$NbTe_2$, Chin. Phys. Lett. 42(6), 067501 (2025).

[187] Y. Ding, and Y. Wang, Intrinsic ferromagnetism and valley polarization in hydrogenated group V transition-metal dinitride (MN_2H_2, M = V/Nb/Ta) nanosheets: insights from first-principles, *Nanoscale* 12(2), 1002 (2020).

[188] N. Wang, J. Zhang, W. Liu, X. Chen, W. Ji, C. Zhang, S. Yan, Y. Wang, and S. Li, Giant valley polarization in Janus 1T-MNY(M = Mo, W; Y = Br, Cl) monolayers: a new class of ferrovalley materials, *Phys. Chem. Chem. Phys.* 28(8), 5359 (2026).

[189] J. Zhao, T. Zhang, R. Peng, Y. Dai, B. Huang, and Y. Ma, Spontaneous Valley Polarization and Electrical Control of Valley Physics in Single-Layer $TcIrGe_2S_6$, *J. Phys. Chem. Lett.* 13(37), 8749 (2022).

[190] K. Sheng, B. Zhang, H. K. Yuan, and Z. Y. Wang, Strain-engineered topological phase transitions in ferrovalley 2H-$RuCl_2$ monolayer, *Phys. Rev. B* 105(19), 195312 (2022).

[191] S. D. Guo, P. Li, and G. Wang, First-principles calculations study of valley polarization in antiferromagnetic bilayer systems, *Phys. Rev. B* 111(14), L140404 (2025).

[192] H. Sun, S. S. Li, W. X. Ji, C. W. Zhang, Valley-dependent topological phase transition and quantum anomalous valley Hall effect in single-layer RuClBr, *Phys. Rev. B* 105(19), 195112 (2022).

[193] Z. Zhang, H. Huang, L. Wang, Y. Zhao, C. Liu, S. Zhou, Y. Wu, J. Zhao, G. Qiao, D. Wang, J. Zhang, X. Zheng, and S. Wang, Strain-explorable valley-polarized

topological phase transition and perpendicular magnetocrystalline anisotropy in hexagonal MClBr(M = Ru, Os) monolayers, *Phys. Rev. B* 110(3), 035128 (2024).

[194] Y. Tian, C. B. Wang, L. Li, X. Kong, and W. J. Gong, Multiferroic properties and the layer-stacking quantum anomalous Hall effect in two-dimensional RuOHX (X = F, Cl, Br), *Appl. Phys. Lett.* 125(17), 173101 (2024).

[195] W. Zhang, J. Zhang, W. Ji, M. Ren, Y. Wang, S. Li, and S. Yan, p-orbital-dependent ferrovalley characteristic in MXene $Lu_3N_2O_2$, *Appl. Phys. Lett.* 125(25), 252403 (2024).

[196] C. S. Hu, Y. J. Wu, Y. S. Liu, S. Fu, X. N. Cui, Y. H. Wang, and C. W. Zhang, Single-layer intrinsic 2H-phase LuX_2 (X = Cl, Br, I) with large valley polarization and anomalous valley Hall effect, *Chin. Phys. B* 32(3), 037306 (2023).

[197] J. Lu, H. Chen, X. Zhao, G. Hu, X. Yuan, and J. Ren, Chiral breathing-valley locking in two-dimensional kagome lattice Ta_3I_8, *Appl. Phys. Lett.* 124(7), 072101 (2024).

[198] G. Zheng, S. Qu, W. Zhou, and F. Ouyang, Janus monolayer TaNF: A new ferrovalley material with large valley splitting and tunable magnetic properties, *Fornt. Phys.* 18(5), 53302 (2023).

[199] N. Wang, J. Zhang, W. Liu, X. Chen, W. Ji, C. Zhang, S. Yan, Y. Wang, and S. Li, Giant valley polarization in Janus 1T-MNY (M = Mo, W; Y = Br, Cl) monolayers: a new class of ferrovalley materials, *Phys. Chem. Chem. Phys.* 28(8), 5359 (2026).

[200] J. Li, X. Cheng, and H. Zhang, Strain-Driven Topological Phase Transition in the $OsCl_2$ Ferrovalley Semiconductor, *J. Phys. Chem. C* 129(40), 18172 (2025).

[201] K. Jia, X. J. Dong, S. S. Li, W. X. Ji, and C. W. Zhang, Electronic-correlation induced sign-reversible Berry phase and quantum anomalous valley Hall effects in Janus monolayer OsClBr, *Phys. Chem. Chem. Phys.* 25(23), 15767 (2023).

[202] H. Liu, J. Li, J. Tian, Y. Li, and J. Shi, Spontaneous and tunable valley polarization in two-dimensional single-layer $LaCl_2$, *Semicond. Sci. Technol.* 39(7), 075006 (2024).

[203] A. Sharan, and N. Singh, Intrinsic Valley Polarization in Computationally Discovered Two-Dimensional Ferrovalley Materials: LaI_2 and PrI_2 Monolayers, *Adv. Theory Simul.* 5(4), 2100476 (2022).

[204] S. Li, Y. Hou, M. Zhou, F. Zheng, X. Shao, and P. Zhang, First-principles prediction of the two-dimensional intrinsic ferrovalley material CeX_2(X = F, Cl, Br), *J. Appl. Phys.* 134(21), 213901 (2023).

[205] Y. Chen, X. Zhao, and Y. An, Prediction for an intrinsic ferrovalley semiconductor in a Janus 2H-CeBrCl monolayer with a high Curie temperature and perpendicular magnetic anisotropy, *Phys. Rev. B* 109(12), 125421 (2024).

[206] Y. Liu, L. Zhang, Z. Xu, S. Fan, and G. Gao, Room-temperature bipolar ferrovalley semiconductors and anomalous valley Hall effect in Janus CeClI and CeBrI, *Mater. Today Phys.* 55(1), 101743 (2025).

[207] X. Wang, L. Liu, N. Wang, Y. Chen, T. Song, Z. Liu, and X. Cui, First-Principles Study on Valley Polarization of Ferromagnetic $PrBr_2$ Monolayer under Strain, *J. Phys. Chem. C* 128(16), 6897 (2024).

[208] X. Wang, L. Liu, N. Wang, Y. Chen, T. Song, Z. Liu, Y. Xing, and X. Cui, Giant Valley Polarization in Bipolar Ferromagnetic Semiconductors SmX_2(X = Cl, Br, I) Monolayers under Strain, *J. Phys. Chem. C* 129(49), 21751 (2025).

[209] K. Sheng, H. K. Yuan, and Z. Y. Wang, Monolayer gadolinium halides, GdX_2(X = F, Cl, Br): intrinsic ferrovalley materials with spontaneous spin and valley polarizations, *Phys. Chem. Chem. Phys.* 24(6), 3865 (2022).

[210] C. Li, and Y. An, Two-dimensional rare-earth Janus 2H-GdXY (X, Y = Cl, Br, I; X ≠ Y) monolayers: Bipolar ferromagnetic semiconductors with high Curie temperature and large valley polarization, *Phys. Rev. B* 107(11), 115428 (2023).

[211] H. J. Zhang, Y. Tian, C. Jiang, J. L. Cai, T. Jin, and L. L. Zhang, Two-dimensional ferromagnetic semiconductor monolayers TbXH (X = Br, Cl, I): Results of first-principles calculations, *Phys. Rev. B* 111(6), 064108 (2025).

[212] J. Y. Li, A. D. Fan, Y. K. Wang, Y. Zhang, and S. Li, Strain-induced valley polarization, topological states, and piezomagnetism in two-dimensional altermagnetic V_2Te_2O, V_2STeO, V_2SSeO, and V_2S_2O, *Appl. Phys. Lett.* 125(22), 222404 (2024).

[213] C. Chen, X. He, Q. Xiong, C. Quan, H. Hou, S. Ji, J. Yang, and X. Li, Strain-modulated valley polarization and piezomagnetic effects in altermagnetic Cr_2S_2, *Appl. Phys. Lett.* 127(10), 102409 (2025).

[214] I. Khan, D. Bezzerga, B. Marfou, and J. Hong, Altermagnetism, piezovalley, and ferroelectricity in two-dimensional Cr_2SeO altermagnet, *npj 2D Mater. Appl.* 9(1), 18 (2025).

[215] S. D. Guo, X. S. Guo, and G. Wang, Valley polarization in two-dimensional tetragonal altermagnetism, *Phys. Rev. B* 110(18), 184408 (2024).

[216] Q. Shen, W. Liao, H. Bao, D. Xu, J. Tan, J. Dong, and G. Ouyang, Tunable valley polarization and spin splitting in altermagnetic $Fe_2MoS_2X_2$ (X = S, Se, Te) via symmetry engineering, *Phys. Rev. Mater.* 9(11), 114404 (2025).

[217] C. Y. Tan, Z. F. Gao, H. C. Yang, Z. X. Liu, K. Liu, P. J. Gao, and Z. Y. Lu, Crystal valley Hall effect, *Phys. Rev. B* 111(9), 094411 (2025).

[218] Y. Liu, J. Li, H. Lian, X. Yao, and X. Zhang, Piezovalley effect in altermagnetic Fe_2WS_4 and $Fe_2WS_2Se_2$ monolayers, *Appl. Phys. Lett.* 128(10), 102402 (2026).

[219] W. Xie, X. Xu, Y. Yue, H. Xia, and H. Wang, Piezovalley effect and magnetovalley coupling in altermagnetic semiconductors studied by first-principles calculations, *Phys. Rev. B* 111(13), 134429 (2025).

[220] Y. Jiang, X. Zhang, H. Bai, Y. Tian, B. Zhang, W. J. Gong, and X. Kong, Strain-engineering spin-valley locking effect in altermagnetic monolayer with multipiezo properties, *Appl. Phys. Lett.* 126(5), 053102 (2025).

[221] J. Zhu, Y. Zhang, M. Wan, J. Shao, Z. Zeng, X. Huang, G. Liu, and D. Huang, Theoretical investigation of altermagnetic materials with tunable valley polarization in monolayer Nb_2Cl_2, *J. Mater. Chem. C* 14(12), 5103 (2026).

[222] S. D. Guo, L. Zhang, X. S. Guo, and G. Zhu, Weak valley-layer coupling and valley polarization in a centrosymmetric 1T-$FeCl_2$ monolayer, *Phys. Rev. B* 112(1), 014453 (2025).

[223] A. Grigoriev, D. H. Do, D. M. Kim, C. B. Eom, B. Adams, E. M. Dufresne, and P. G. Evans, Nanosecond

Domain Wall Dynamics in Ferroelectric $Pb(Zr,Ti)O_3$ Thin Films, *Phys. Rev. Lett.* 96(18), 187601 (2006).
[224] A. Gruverman, D. Wu, and J. F. Scott, Piezoresponse Force Microscopy Studies of Switching Behavior of Ferroelectric Capacitors on a 100-ns Time Scale, *Phys. Rev. Lett.* 100(9), 097601 (2008).
[225] B. Liu, X. Li, J. Feng, C. Xu, and H. Xiang, Unraveling atomistic and electronic origins of multiaxial magnetic anisotropy, *Sci. China Phys. Mech. Astron.* 68(2), 227511 (2025).
[226] S. D. Guo, Hidden altermagnetism, *Front. Phys.* 21(2), 025201 (2026).
[227] S. Zhang, P. Chang, Y. Zhang, X. Xu, L. Guan, an J. Tao, Effect of morphology and stacking on atomic interaction and magnetic characteristics in two-dimensional H-phase VS_2 few layers, *J. Mater. Sci.* 57(10), 5873 (2022).
[228] X. Wang, D. Li, Z. Li, C. Wu, C. M. Che, G. Chen, and X. Cui, Ferromagnetism in 2D Vanadium Diselenide, *ACS Nano* 15(10), 16236 (2021).
[229] S. Duan, J. Gou, Z. Cai, J. Hu, Y. Wang, H. R. Tan, M. Lin, J. Zhang, B. Feng, K. P. Loh, F. Zheng, A. T. S. Wee, and W. Chen, Doping-tunable charge ordering in semiconducting single-layer Cr_2Se_3, *Sci. Adv.* 11(36), eadx8310 (2025).
[230] M. K. Kinyanjui, J. Koester, F. Boucher, A. Wildes, and U. Kaiser, Spectroscopic properties of a freestanding $MnPS_3$ single layer, *Phys. Rev. B* 98(3), 035417 (2018).
[231] H. Wang, X. Huang, J. Lin, J. Cui, Y. Chen, C. Zhu, F. Liu, Q. Zeng, J. Zhou, P. Yu, X. Wang, H. He, S. H. Tsang, W. Gao, K. Suenaga, F. Ma, C. Yang, L. Lu, T. Yu, E. H. T. Teo, G. Liu, and Z. Liu, High-quality monolayer superconductor $NbSe_2$ grown by chemical vapour deposition, *Nat. Commun.* 8(1), 394 (2017).
[232] N. Gauriot, R. Pandya, J. A. Webber, and A. Rao, Isolation and characterization of monolayer phosphorene analogues, *J. Phys.: Condens. Matter* 37(3), 03LT01 (2025).
[233] H. Lin, J. Si, X. Zhu, K. Cai, H. Li, L. Kong, X. Yu, and H. H. Wen, Structure and physical properties of $CsV_2Se_{2-x}O$ and V_2Se_2O, *Phys. Rev. B* 98(7), 075132 (2018).
[234] B. Huang, C. Gui, A. Zhang, Z. Yang, S. Z. Li, Z. Li, H. Li, and W. B. Zhang, Toward a unified description of valley polarization in two-dimensional tetragonal altermagnets driven by strain and in-plane magnetization, *Phys. Rev. B* 114(4), 045421 (2026).
[235] J. Y. Zhan, R. He, D. Wang, M. D. He, N. Luo, J. Zeng, K. Q. Chen, and L. M. Tang, Multiphysics field driven valley polarization in tetragonal altermagnets, *Phys. Rev. B* 112(2), 024408 (2025).
[236] S. Chen, M. Ge, H. Chen, J. Tan, and G. Ouyang, Tunable valley-contrasting Rashba effect and spatially disentangled photocurrents in Janus altermagnetic $Mn_2P_2X_3Y_3$ monolayers, *Phys. Rev. B* 114(4), 045426 (2026).
[237] R. W. Zhang, C. Cui, R. Li, J. Duan, L. Li, Z. M. Yu, and Y. Yao, Predictable Gate-Field Control of Spin in Altermagnets with Spin-Layer Coupling, *Phys. Rev. Lett.* 133(5), 056401 (2024).
[238] Z. Zhang, H. Sun, M. Dong, Y. Guo, and M. Zhao, Giant valley splitting and tunable anisotropic spin plasmons in a Janus ferrovalley monolayer, *npj Comput. Mater.* 11(1), 277 (2025).
[239] W. Chen, Z. Sun, Z. Wang, L. Gu, X. Xu, S. Wu, and C. Gao, Direct observation of van der Waals stacking-dependent interlayer magnetism, *Science* 366(6468), 983 (2019).
[240] N. Sivadas, S. Okamoto, X. Xu, C. J. Fennie, and D. Xiao, Stacking-Dependent Magnetism in Bilayer CrI_3, *Nano Lett.* 18(12), 7658 (2018).
[241] X. Li, X. Xu, H. Zhou, H. Jia, E. Wang, H. Fu, J. T. Sun, and S. Meng, Tunable topological states in stacked chern insulator bilayers, *Nano Lett.* 23(7), 2839 (2023).
[242] L. Li, and M. Wu, Binary compound bilayer and multilayer with vertical polarizations: two-dimensional ferroelectrics, multiferroics, and nanogenerators, *ACS Nano* 11(6), 6382 (2017).
[243] K. Yasuda, X. Wang, K. Watanabe, T. Taniguchi, and P. Jarillo-Herrero, Stacking-engineered ferroelectricity in bilayer boron nitride, *Science* 372(6549), 1458 (2021).
[244] J. Tian, X. Zhou, and G. B. Liu, Layer-mediated tuning of spin and valley physics in stacked tetragonal altermagnetic bilayers, *Phys. Rev. B* 114(9), 094422 (2026).
[245] M. Ali, M. U. Muzaffar, B. Ali, M. Fayaz, and Z. Lin, Sliding-Controlled Switchable In-Plane Altermagnetic Ferrovalley States and Strong Optical Response in Cr_2WS_4 for Applications in Valleytronic Devices, *ACS Appl. Nano Mater.* 9(28), 13568 (2026).
[246] Y. Q. Li, Y. K. Zhang, X. L. Lu, Y. P. Shao, Z. Q. Bao, J. D. Zheng, W. Y. Tong, and C. G. Duan, Ferrovalley Physics in Stacked Bilayer Altermagnetic Systems, *Nano Lett.* 25(15), 6032 (2025).
[247] Y. Chen, H. Lv, X. Wu, and J. Yang, Bilayer Metal-Organic Framework Altermagnets with Electrically Tunable Spin-Split Valleys, *J. Am. Chem. Soc.* 147(17), 14806 (2025).
[248] J. J. Hauser, Magnetic proximity effect, *Phys. Rev.* 187(2), 580 (1969).
[249] A. I. Buzdin, Proximity effects in superconductorferromagnet heterostructures, *Rev. Mod. Phys.* 77(3), 935 (2005).
[250] A. M. Alsharari, M. M. Asmar, and S. E. Ulloa, Proximity-induced topological phases in bilayer graphene, *Phys. Rev. B* 97(24), 241104(R) (2018).
[251] K. H. Jin, and S. H. Jhi, Proximity-induced giant spin-orbit interaction in epitaxial graphene on a topological insulator, *Phys. Rev. B* 87(7), 075442 (2013).
[252] Z. Zhu, R. Huang, X. Chen, Z. Cui, X. Duan, J. Zhang, I. Zutic, and T. Zhou, Altermagnetic Proximity Effect, *Phys. Rev. Lett.* 136(18), 186702 (2026).
[253] W. Xie, L. Wang, X. Xu, Y. Yue, H. Xia, L. He, and H. Wang, Realizing giant valley polarization effect based on monolayer altermagnets, *Acta Phys. Sin.* 74(22), 227502 (2025).
[254] W. Xie, Y. Chen, Y. Sun, X. Xu, Y. Yue, and H. Wang, Magnetic proximity-induced non-relativistic valley polarization, arXiv: 2607.22360.
[255] Z. Liang, J. Zhang, Y. Wang, C. Hua, and F. Song, Spin-valley splitting in altermagnet/ferromagnet $Ca(CoN)_2/CoX$ (X = Cl_2, Se) heterostructures, *Phys. Rev. B* 113(18), 184434 (2026).
[256] Y. Q. Li, W. Y. Tong, and C. G. Duan, Altermagnetic ferrovalley materials: Paradigm shift and frontier advances in valleytronics, *Front. Phys.* 21(7), 075302 (2026).

[257] H. Lin, J. Si, X. Zhu, K. Cai, H. Li, L. Kong, X. Yu, and H. H. Wen, Structure and physical properties of $CsV_2Se_{2-x}O$ and V_2Se_2O, *Phys. Rev. B* 98(7), 075132 (2018).

ABSTRACT FIGURE

